Remote Sensing of Environment 285 (2023) 113415

Contents lists available at ScienceDirect

Remote Sensing of Environment

journal homepage: www.elsevier.com/locate/rse

Coupling ecological concepts with an ocean-colour model: Phytoplankton size structure

Xuerong Sun [a,*], Robert J.W. Brewin [a], Shubha Sathyendranath [b,c], Giorgio Dall'Olmo [d], Ruth Airs [b], Ray Barlow [e], Astrid Bracher [f,g], Vanda Brotas [h,b,i], Malika Kheireddine [j], Tarron Lamont [k,e,l], Emilio Marañón [m], Xosé Anxelu G. Morán [n,j], Dionysios E. Raitsos [o], Fang Shen [p], Gavin H. Tilstone [b]

[a] Centre for Geography and Environmental Science, Department of Earth and Environmental Science, Faculty of Environment, Science and Economy, University of Exeter, Cornwall, United Kingdom
[b] Plymouth Marine Laboratory, Plymouth, Devon, United Kingdom
[c] National Centre for Earth Observation, Plymouth Marine Laboratory, Plymouth, Devon, United Kingdom
[d] Istituto Nazionale di Oceanografia e di Geofisica Sperimentale - OGS, Trieste, Italy
[e] Bayworld Centre for Research & Education, Cape Town, South Africa
[f] Phytooptics, Alfred Wegener Institute, Helmholtz Centre for Polar and Marine Research, Bremerhaven, Germany
[g] Institute of Environmental Physics, University of Bremen, Bremen, Germany
[h] MARE – Marine and Environmental Science Centre, Faculdade de Ciências, Universidade de Lisboa, Lisbon, Portugal
[i] Departamento de Biologia Vegetal, Faculdade de Ciências, Universidade de Lisboa, Lisbon, Portugal
[j] Division of Biological and Environmental Sciences and Engineering, Red Sea Research Center, King Abdullah University for Science and Technology, Thuwal, Saudi Arabia
[k] Oceans & Coasts Research, Department of Forestry, Fisheries & Environment, Cape Town, South Africa
[l] Department of Oceanography, University of Cape Town, South Africa
[m] Department of Ecology and Animal Biology, Universidade de Vigo, Vigo, Spain
[n] Centro Oceanográfico de Gijón/Xixón (IEO,CSIC), Gijón/Xixón, Spain
[o] Department of Biology, National and Kapodistrian University of Athens, Athens, Greece
[p] State Key Laboratory of Estuarine and Coastal Research, East China Normal University, Shanghai, China

ARTICLE INFO

Edited by Menghua Wang

Keywords:
Ocean-colour model
Climate change
Phytoplankton size classes
HPLC pigments
Size-fractionated fluorometric
Ocean-colour remote sensing

ABSTRACT

Phytoplankton play a central role in the planetary cycling of important elements and compounds. Understanding how phytoplankton are responding to climate change is consequently a major question in Earth Sciences. Monitoring phytoplankton is key to answering this question. Satellite remote sensing of ocean colour is our only means of monitoring phytoplankton in the entire surface ocean at high temporal and large spatial scales, and the continuous ocean-colour data record is now approaching a length suitable for addressing questions around climate change, at least in some regions. Yet, developing ocean-colour algorithms for climate change studies requires addressing issues of ambiguity in the ocean-colour signal. For example, for the same chlorophyll-a concentration (Chl-a) of phytoplankton, the colour of the ocean can be different depending on the type of phytoplankton present. One route to tackle the issue of ambiguity is by enriching the ocean-colour data with information on sea surface temperature (SST), a good proxy of changes in three phytoplankton size classes (PSCs) independent of changes in total Chl-a, a measure of phytoplankton biomass. Using a global surface *in-situ* dataset of HPLC (high performance liquid chromatography) pigments, size-fractionated filtration data, and concurrent satellite SST spanning from 1991 to 2021, we re-tuned, validated and advanced an SST-dependent three-component model that quantifies the relationship between total Chl-a and Chl-a associated with the three PSCs (pico-, nano- and microplankton). Similar to previous studies, striking dependencies between model parameters and SST were captured, which were found to improve model performance significantly. These relationships were applied to 40 years of monthly composites of satellite SST, and significant trends in model parameters were observed globally, in response to climate warming. Changes in these parameters highlight issues in estimating long-term trends in phytoplankton biomass (Chl-a) from ocean colour using standard empirical algorithms, which implicitly assume a fixed relationship between total Chl-a and Chl-a of the three

* Corresponding author.
E-mail address: x.sun8@exeter.ac.uk (X. Sun).

https://doi.org/10.1016/j.rse.2022.113415
Received 27 April 2022; Received in revised form 25 November 2022; Accepted 7 December 2022

size classes. The proposed ecological model will be at the centre of a new ocean-colour modelling framework, designed for investigating the response of phytoplankton to climate change, described in subsequent parts of this series of papers.

1. Introduction

Climate change is arguably the biggest environmental and ecological concern mankind has faced in the last century and is among the greatest threats to life on our planet (Dow and Downing, 2016). The ocean covers approximately 71% of the Earth's surface, comprises around 99% of the biosphere, and modulates the pace and extent of climate change. Sea surface temperature (SST) is expected to rise between 1.5 to 4.0 °C by the end of this century relative to pre-industrial times (Rhein et al., 2013). Ongoing climate change is expected to cause ocean warming, acidification, oxygen loss, reduced near-surface nutrients, and lower ocean primary production (Bindoff et al., 2019). Climate change is consequently modifying the physical and chemical structure of the ocean with profound consequences for pelagic ecosystems (Hoegh-Guldberg and Bruno, 2010). As a critical component of the Earth's system, phytoplankton operate at the base of the marine food web and are responsible for ~ 50% of global primary production (Longhurst et al., 1995; Field et al., 1998). They provide key services in climate regulation through their critical role in the global carbon cycle (Cermeño et al., 2008) and the cycling of other key elements and compounds (e.g. nitrogen and phosphorus, Falkowski et al., 1998). Given the central position of phytoplankton in the pelagic ecosystem, understanding how phytoplankton are responding to climate change is among the most pressing questions in biological oceanography (Hays et al., 2005).

Answering this question requires monitoring techniques capable of making quantitative observations of oceanic phytoplankton synoptically, at high spatial and temporal resolution (Lombard et al., 2019), and that meet the need for sufficient measurement stability over the long term (Henson et al., 2010). Prior studies have investigated the response of phytoplankton to climate change using historical *in-situ* data records that are limited in spatial and temporal coverage (Boyce et al., 2010; Wernand et al., 2013), or through laboratory and/or mesocosm experiments (Schaum et al., 2017), which are not always representative of natural conditions or global in scope. At present, satellite remote sensing of ocean colour is the only tool available that provides information on surface ocean phytoplankton at high spatial and temporal resolution, and is therefore recognised as the main source of data for assessing changes in phytoplankton globally (McClain, 2009; Siegel and Franz, 2010; Sathyendranath et al., 2019). Furthermore, we are now approaching a point in time when we have a continuous ocean-colour record that is sufficient in length to investigate the impact of climate change on phytoplankton, at least in some areas of the ocean (Hammond et al., 2020).

The influence of climate change on surface oceanic phytoplankton can manifest in different ways, for example, through changes in phytoplankton phenology (Kahru et al., 2010; Gittings et al., 2018), biomass (Martinez et al., 2009; Boyce et al., 2010), primary production (Behrenfeld et al., 2006; Gregg and Rousseaux, 2019; Kulk et al., 2020), and community composition (Sharma et al., 2019; Sun et al., 2019). Satellite ocean-colour algorithms need to be tailored to detect these responses to climate change (Sathyendranath et al., 2017). One of the major challenges to using ocean-colour data for detecting information on phytoplankton is the problem of ambiguity (Defoin-Platel and Chami, 2007). For example, for the same total chlorophyll-a concentration (Chl-a), i.e., a measure of phytoplankton biomass, the colour of the ocean can be different depending on the amount of other optically active constituents present in water (e.g., non-algal particles (NAP), coloured dissolved organic matter (CDOM)). Similarly, for the same Chl-a, the colour of the ocean can be different depending on the type (e.g., size) of phytoplankton present in the water, due to different pigment compositions and inherent optical properties (Sathyendranath et al., 2001; Alvain et al., 2005; Dierssen, 2010; Brewin et al., 2019a). Standard phytoplankton Chl-a algorithms, which are widely used by space agencies (e.g., OC4, O'Reilly et al., 1998), assume that these optical constituents (i.e., phytoplankton, NAP, CDOM) and phytoplankton type co-vary in a predictable manner with Chl-a (Brewin et al., 2014b). However, in the context of climate change, optically-active water constituents may be changing in different ways, for example, total and group-specific phytoplankton absorption have been found to vary with changes in SST (Brewin et al., 2019a), making standard algorithms unsuitable for detecting long-term trends in phytoplankton biomass. Consequently, there is an urgent requirement to develop ocean-colour algorithms which are robust to the effects of climate change (Sathyendranath et al., 2017).

The extent of the ambiguity problem depends somewhat on the spectral properties (e.g., spectral resolution and bandwidths) of the ocean-colour data. Hyperspectral ocean colour (generally with > 20 wavebands and < 15 nm bandwidths in the visible region of the electromagnetic spectrum) is thought to contain more independent information than multispectral data (usually with 3–10 wider wavebands in the visible and infrared electromagnetic spectrum), which makes the problem less ambiguous (Lubac et al., 2008; Torrecilla et al., 2011). There are new and exciting hyperspectral sensors in orbit now (e.g., DESIS [DLR Earth Sensing Imaging Spectrometer], Gaofen-5, PRISMA [PRecursore IperSpettrale della Missione Applicativa], EnMAP [Environmental Monitoring and Analysis Program]) or expected to be in orbit in the near future (e.g., PACE [Plankton, Aerosol, Cloud, ocean Ecosystem], CHIME [Copernicus Hyperspectral Imaging Mission for the Environment]) (Dierssen et al., 2021, and references therein). Hyperspectral satellite sensors have proven effective for detecting several major phytoplankton groups (Bracher et al., 2009; Losa et al., 2017), and time series data from 2002 to 2012 have been produced using SCIAMACHY data (SCanning Imaging Absorption spectroMeter for Atmospheric CartograpHY, Bracher et al., 2017). However, long-term records of hyperspectral ocean-colour data, of sufficient length for climate-change studies, do not currently exist. Another potential solution to the ambiguity problem is through the use of the fluorescence signal of pigments. The fluorescence signal, which can be detected by some ocean-colour sensors, is known to be phytoplankton-type-dependent (Suggett et al., 2009), and impacted by primary production and the structure of photosystems in the cells (Sathyendranath et al., 2004). However, the signal is highly complex to interpret and is small in most parts of the ocean (oligotrophic waters). A common approach to tackle the problem of ambiguity is through enrichment strategies, involving the use of ancillary information that is independent of ocean colour (Defoin-Platel and Chami, 2007).

Previous studies have shown that the relationship between phytoplankton biomass (Chl-a) and size structure is sensitive to environmental conditions (e.g., temperature and light, Brewin et al., 2015, 2017; Ward, 2015; Moore and Brown, 2020). For example, temperature has a direct influence on phytoplankton size structure by impacting the physiological properties of phytoplankton (e.g., uptake rates of nutrients, López-Urrutia and Morán, 2015), or an indirect control through the covariation of temperature and resource supply (e.g., nutrients, light, Marañón et al., 2015; Brewin et al., 2017). Among these environmental variables, SST can be retrieved from thermal and microwave

remote sensing with high accuracy, with records spanning from 1981 to the present day (Minnett et al., 2019), covering the whole ocean-colour satellite time series. Furthermore, there is evidence that by including SST as an explanatory independent variable in empirical algorithms of ocean colour, which relate the ratio of blue–green reflected light to Chl-a, model performance can be improved (Gholizadeh and Robeson, 2016). It has also been demonstrated that the relationship between phytoplankton absorption and Chl-a can be improved by including information on temperature (Bouman et al., 2003; Brewin et al., 2019a), and that temperature can be used to accurately estimate size-fractionated photosynthesis-irradiance parameters (Robinson et al., 2018).

Here, we present the first part of a series of papers with the aim of providing a new global theoretical ocean-colour model framework, which explicitly incorporates the influence of SST on the relationship between phytoplankton biomass (i.e., Chl-a) and size structure. In this first paper, we compile a large worldwide *in-situ* dataset of total and size-fractionated Chl-a with concurrent SST data, and then re-tune and advance an existing SST-dependent model of phytoplankton size structure (Brewin et al., 2017) for global application. We observe striking patterns between the parameters of the model and SST, in support of earlier regional studies. Using an independent validation dataset, we test and compare the performance of the proposed models with those from previous studies. Then, we investigate how the parameters of the SST-dependent model may have changed over the past 40 years using the satellite SST data record, in view of how the marine ecosystem is responding to climate change. The ecological model presented here is at the heart of a new theoretical ocean-colour model which will be described in the subsequent parts of this series of papers.

2. Data and methods

2.1. In-situ datasets

2.1.1. Size-fractionated chlorophyll-a estimated from HPLC

A total of 34,312 High Performance Liquid Chromatography (HPLC) samples collected from the surface global ocean between 1991 and 2021 were used in this study, spanning from equatorial to polar regions, and covering both oligotrophic oceanic and eutrophic coastal regions (Fig. 1). Table A.1 in the Appendix A defines all the abbreviations and symbols used in the paper. The pigment dataset from Brewin et al. (2015) was updated by adding more published datasets from Western Channel Observatory (Smyth et al., 2009), TARA Ocean (Chase et al., 2013), Rothera Research Station, NASA SeaWiFS Bio-optical Archive and Storage System (SeaBASS, Werdell et al., 2003), Australian Ocean Data Network (AODN, IMOS, 2021a,b), Government of Canada, DataONE (Cota and Hill, 2007a,b; Hill, 2007a,b; DiTullio and Lee, 2019b; Palmer Station Antarctica LTER et al., 2020; Southern California Bight MBON et al., 2021), Biological and Chemical Oceanography Data Management Office (BCO-DMO, McGillicuddy, 2007a,b; DiTullio, 2011, 2015; Vaillancourt and Marra, 2011; Bidigare, 2012; Richardson et al., 2013; DiTullio and Lee, 2019a; Lee, 2020; Landry, 2021), Environmental Data Initiative Data Portal (EDI, Palmer Station Antarctica LERT et al., 2018), PANGAEA (Taylor et al., 2011; Claustre, 2013; Bracher, 2014a,b, 2015a,b,c,d,e, 2019; Clayton et al., 2014; Peeken and Hoffmann, 2014; Peeken and Nachtigall, 2014a,b,c; Bracher et al., 2015, 2020; Hepach et al., 2016; Bracher and Taylor, 2017; Peeken and Quack, 2017; Peeken and Walter, 2017; Peeken et al., 2017a,b,c,d; Taylor and Bracher, 2017; Bracher and Wiegmann, 2019; Liu et al., 2019), and some published works (Sun et al., 2018, 2019, 2022). More detailed information of the *in-situ* HPLC pigment data is shown in Supplementary Table S1. To minimise the spatiotemporal autocorrelation between training and validation datasets and provide more accurate prediction errors (Stock and Subramaniam, 2022, and references therein), the whole dataset are sufficiently separated based on the sampling time (i.e., pre and post 2016). Therefore, 5607 samples in the HPLC dataset collected after 2016 were set aside and used for independent validation, leaving 28,705 samples for model training.

The HPLC samples include concentrations of chlorophyll-a (hereafter denoted Chl-a, representing the sum of monovinyl chlorophyll-a, divinyl chlorophyll-a, and chlorophyllide-a) and seven diagnostic pigments, which are indicative of particular size classes. In this study, only samples collected within the top 20 m (within the surface mixed layer depth, de Boyer Montégut et al., 2004) of the water column were used (Brewin et al., 2017). For stations with multiple observations within the top 20 m depth, each sample is treated as a discrete measurement (rather than being averaged). To control the quality of the pigment data, HPLC data for which Chl-a lower than 0.001 mg m^{-3} were removed, and diagnostic pigments lower than 0.001 mg m^{-3} were set to zero (Claustre et al., 2004; Uitz et al., 2006). HPLC data were retained only if the difference between the total chlorophyll concentration and the total accessory pigments concentration was less than 30% of the total pigment concentration (Aiken et al., 2009).

The fractions of Chl-a for three phytoplankton classes (i.e., picoplankton (< 2 μm), nanoplankton (2–20 μm), microplankton (> 20 μm), Sieburth et al., 1978), were calculated using diagnostic pigment analyses (Vidussi et al., 2001; Uitz et al., 2006; Brewin et al., 2010; Hirata et al., 2011). The total chlorophyll-a concentration, C_w, was estimated from the weighted sum of seven diagnostic pigments, according to,

$$C_w = \sum_{i=1}^{7} W_i P_i, \tag{1}$$

where W and P are the weights and the corresponding diagnostic pigments respectively, with i = fucoxanthin, peridinin, 19'-hexanoyloxy fucoxanthin, 19'-butanoyloxyfucoxanthin, alloxanthin, total chloro phyll-b, and zeaxanthin. The weights were computed using multilinear regression on the training dataset (N = 28,705) in $\log_{10}$ space (as data distribution close to log-normal), as shown in Table 1. The values of weights are comparable with previous studies in the global ocean (Uitz et al., 2006; Brewin et al., 2015), and C_w are in good agreement with the *in-situ* Chl-a (C), with the correlation and root mean squared difference ($\log_{10}$-transformed) at 0.982 and 0.111, respectively. Supplementary Figures S1a and S1b show that differences in weights between the training dataset and the whole dataset were small. Therefore, weights calculated from the training dataset were used for the validation dataset, making the datasets fully independent.

Following Brewin et al. (2015), fractions of PSCs to total Chl-a were computed using the following equations,

$$F_1 = \begin{cases} \frac{(-12.5C + 1)W_3 P_3}{C_w} + \frac{\sum_{i=6}^{7} W_i P_i}{C_w} & \text{if } C \le 0.08 \text{ mg m}^{-3} \\ \frac{\sum_{i=6}^{7} W_i P_i}{C_w} & \text{if } C > 0.08 \text{ mg m}^{-3}, \end{cases} \tag{2}$$

$$F_2 = \begin{cases} \frac{12.5CW_3 P_3}{C_w} + \frac{\sum_{i=4}^{5} W_i P_i + W_1 P_{1,n}}{C_w} & \text{if } C \le 0.08 \text{ mg m}^{-3} \\ \frac{\sum_{i=3}^{5} W_i P_i + W_1 P_{1,n}}{C_w} & \text{if } C > 0.08 \text{ mg m}^{-3}, \end{cases} \tag{3}$$

and

$$F_3 = \frac{\sum_{i=1}^{2} W_i P_i - W_1 P_{1,n}}{C_w}, \tag{4}$$

where F_1, F_2, and F_3 represent fractions of picoplankton, nanoplankton, and microplankton, respectively. As fucoxanthin is also present in nanoplankton, part of the fucoxanthin pigment was apportioned to the nanoplankton pool (Devred et al., 2011), $P_{1,n}$, which was computed according to

$$P_{1,n} = 10^{q_1 \log_{10}(P_3) + q_2 \log_{10}(P_4)}, \tag{5}$$

where P_3 and P_4 refer to 19'-hexanoyloxyfucoxanthin and 19'-butanoyloxyfucoxanthin, and coefficients q_1 and q_2 were computed using the training dataset in $\log_{10}$ space, as shown in Table 1. Note that when $P_{1,n}$ exceeded P_1, the $P_{1,n}$ was set equal to P_1. Consistency in $P_{1,n}$ when

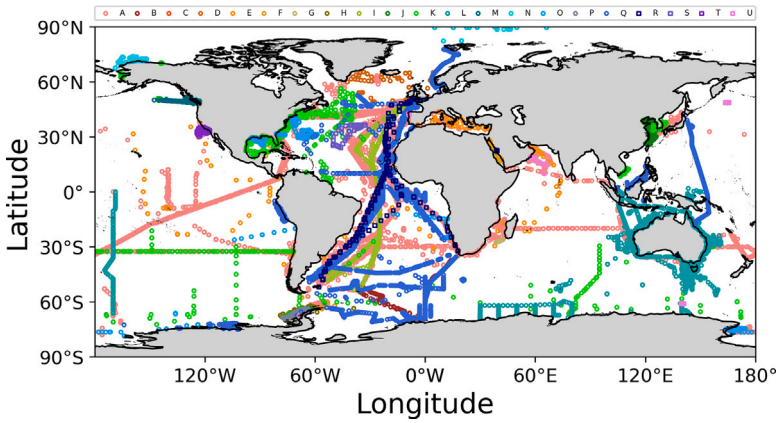

Fig. 1. Locations of *in-situ* datasets used in this study, including two independent datasets of HPLC pigments (circles, N = 34,312) and size-fractionated filtration (squares, N = 2278), N = 36,590. The letters A–U represent the sources of data, which can be found in Supplementary Table S1. (For interpretation of the references to colour in this figure legend, the reader is referred to the web version of this article.)

Table 1
Weights of the seven pigments for diagnostic pigment analyses and coefficients of two pigments for the fucoxanthin adjustment used in this study and in previous studies (Uitz et al., 2006; Devred et al., 2011; Brewin et al., 2015). Bracketed values refer to the standard deviations for each weight and coefficient. Note that weights and coefficients derived from the whole dataset were included only for comparison. Additional results associated with the Table can be found in Supplementary Figure S1.

Pigments	Weights				
	W_i	This study (Training dataset)	This study (Whole dataset)	Brewin et al. (2015) (Global Ocean)	Uitz et al. (2006) (Global Ocean)
Fucoxanthin (P_1)	W_1	1.74 (0.01)	1.75 (0.01)	1.51 (0.01)	1.41
Peridinin (P_2)	W_2	1.52 (0.03)	1.46 (0.02)	1.35 (0.02)	1.41
19'-Hexanoyloxyfucoxanthin (P_3)	W_3	1.24 (0.01)	1.20 (0.01)	0.95 (0.01)	1.27
19'-Butanoyloxyfucoxanthin (P_4)	W_4	0.55 (0.03)	0.60 (0.03)	0.85 (0.02)	0.35
Alloxanthin (P_5)	W_5	1.76 (0.02)	1.78 (0.02)	2.71 (0.05)	0.60
Total chlorophyll-b (P_6)	W_6	1.78 (0.02)	1.84 (0.02)	1.27 (0.01)	1.01
Zeaxanthin (P_7)	W_7	1.04 (0.01)	1.05 (0.01)	0.93 (0.00)	0.86
Pigments	Coefficients				
	q_i	This study (Training dataset)	This study (Whole dataset)	Brewin et al. (2015) (Global Ocean)	Devred et al. (2011) (Global Ocean)
19'-Hexanoyloxyfucoxanthin (P_3)	q_1	0.31 (0.01)	0.43 (0.01)	0.356	0.680 (0.074)
19'-Butanoyloxyfucoxanthin (P_4)	q_2	1.16 (0.01)	1.07 (0.01)	1.190	0.680 (0.111)

using different pairs of coefficients from the training dataset and whole dataset is shown in Supplementary Figure S1c. As with the weights, coefficients (q_1 and q_2) calculated from the training dataset were used in our study, resulting in a fully independent dataset for validation. The fractions of each size classes were then multiplied by the corresponding C to derive the size-specific Chl-a for picoplankton (C_1), nanoplankton (C_2), microplankton (C_3), and combined pico- and nanoplankton ($C_{1,2}$).

2.1.2. Size-fractionated filtration data

A total of 2278 size-fractionated fluorometric (SFF) chlorophyll-a measurements collected between 1995 and 2018 were used in this study (Fig. 1). The SFF dataset is composed of samples from previous works (Marañón et al., 2012; Brewin et al., 2014c, 2017, 2019b), the British Oceanographic Data Centre (BODC), and DataONE (California Current Ecosystem LTER and Goericke, 2018; Sosik et al., 2021). More detailed information of the *in-situ* SFF datasets are shown in Supplementary Table S1. In general, the concentration of Chl-a contained in the water sample passing through 2 μm filter is designated C_1 (picoplankton), that passing through the 20 μm filter and retained on the 2 μm filter is designated C_2 (nanoplankton), and that retained on the 20 μm filter is designated C_3 (microplankton). The total chlorophyll-a concentration is the sum of the size fractions for each class. Note that, filters with pore size of 3 μm, rather than 2 μm, were used in the two datasets (California Current Ecosystem LTER and Goericke, 2018; Sosik et al., 2021, N = 1663). Considering that the number of size-fractionated Chl-a estimated from HPLC method is much larger, the influence of these samples with pore size of 3 μm from SFF method on model training and validation is small (or negligible). Similar to the *in-situ* HPLC dataset, only samples collected within the top 20 m of the water column were used, and 404 SFF samples collected after 2016 were set aside for independent validation, leaving 1874 samples for model training.

Through comparing concurrent and co-located total and size-fractionated Chl-a derived from SFF and HPLC pigments, previous studies have observed systematic biases but significant correlations between the two methods (Brewin et al., 2014c,d, 2017). Given the consistent agreement between the influence of SST on the model parameters when fitting the three-component model to HPLC and SFF data separately (see Section 2.4.2), the two *in-situ* datasets were combined into a single global dataset in this study, providing a total of 36,590 measurements of size-fractionated Chl-a for further analysis, of which 30,579 samples collected before 2016 were used for model development and 6011 samples after 2016 for validation. Among the whole dataset (N = 36,590), there are 6624 stations with multiple samples from different depths within the top 20 m of the water column. Supplementary Figure S2 shows that differences in fractions of PSCs between these vertical depths and the shallowest depth are small, with median values of ratios all close to 1, supporting our justification of a surface 20 m layer depth being within the surface mixed-layer for the majority of the data used. Supplementary Figure S3 provides a comprehensive frequency distribution of different variables in the dataset, including the date, geographical location, sample depth, bottom depth, SST, and Chl-a concentration of sampling stations.

2.2. SST datasets

2.2.1. Daily

Daily composites of Optimal Interpolation Sea Surface Temperature (OISST, version 2) data (1/4° resolution), spanning from 1991 to 2021, were obtained from the NOAA website (https://psl.noaa.gov/data/gridded/data.noaa.oisst.v2.highres.html), distributed by the NOAA PSL. Each PSC measurement from the global dataset was paired with the SST data by matching each *in-situ* sample in time (daily temporal match-up) and space (closest latitude and longitude). *In-situ* samples with unrealistic SST (i.e., > 40 °C or < −1.8 °C) were removed prior to analysis. Among the whole *in-situ* size-fractionated Chl-a dataset (N = 36,590), eight datasets have concurrent *in-situ* temperature records (N = 4164) measured by a conductivity–temperature–depth profiler deployed alongside the water samples, including six HPLC pigment datasets (NAAMES2/3/4 cruises from NASA SeaBASS, Clayton et al., 2014; Peeken and Hoffmann, 2014; Brewin et al., 2015; Sun et al., 2018, 2019, 2022; Southern California Bight MBON et al., 2021) and two size-fractionated filtration datasets (Marañón et al., 2012; Brewin et al., 2019b). Supplementary Figure S4 shows that the matched daily OISST data compare reasonably well with *in-situ* temperature measurements, with a high correlation of 0.975. Therefore, to make full use of the size-fractionated Chl-a dataset and ensure a consistent use of SST measurements, daily OISST SST match-ups, instead of *in-situ* temperature measurements, are used in this study for model development and validation.

2.2.2. Monthly

Monthly composites of OISST (version 2) data (1° resolution), spanning from December 1981 to November 2021, were obtained from the NOAA website (https://psl.noaa.gov/data/gridded/data.noaa.oisst.v2.html), and used to illustrate spatial and temporal patterns in the parameters of SST-dependent models.

Monthly composites of SST data (1° resolution) from the ESA Sea Surface Temperature Climate Change Initiative (SST-CCI, Obs4MIPS monthly-averaged sea surface temperature data, v2.1), spanning from September 1981 to December 2017, were also used in this study, which were downloaded from the CEDA Archive website (https://data.ceda.ac.uk/neodc/esacci/sst/data/obs4MIPs/UReading/ESA-CCI-SST-v2-1/mon/tos/gn/v20201130).

2.3. Auxiliary datasets

2.3.1. GEBCO gridded bathymetric dataset

The bathymetric depth of each sample was extracted by matching each *in-situ* sample in space (closest latitude and longitude) with a gridded bathymetric data (GEBCO2021 Grid), acquired from the GEBCO website (https://www.gebco.net/data_and_products/gridded_bathymetry_data/#global). *In-situ* samples with the bottom depth above 0 m sea level elevation were removed prior to analysis.

2.3.2. OC-CCI chlorophyll-a dataset

A monthly climatology of global chlorophyll-a concentration (4 km resolution) from Ocean Colour Climate Change Initiative (OC-CCI, version 5.0, Sathyendranath et al., 2021) was obtained from the OC-CCI website (https://climate.esa.int/en/projects/ocean-colour/), and was used to help illustrate patterns and changes in the parameters of the three-component model.

2.4. Model developments

2.4.1. SST-independent model of Brewin et al. (2010)

The three-component model of Brewin et al. (2010) is designed to estimate fractional contributions of PSCs as a continuous function of Chl-a, which is based on the application of an exponential function, first proposed by Sathyendranath et al. (2001) for two size fractions. The fraction of total Chl-a (C) from combined pico- and nanoplankton ($F_{1,2}$) and from picoplankton (F_1) are expressed as,

$$F_{1,2} = \frac{C^m_{1,2}[1 - \exp(-\frac{D_{1,2}}{C^m_{1,2}}C)]}{C}, \quad (6)$$

and

$$F_1 = \frac{C^m_1[1 - \exp(-\frac{D_1}{C^m_1}C)]}{C}, \quad (7)$$

where parameters $C^m_{1,2}$ and C^m_1 are the asymptotic maximum values, and $D_{1,2}$ and D_1 determine the fractions of Chl-a as total Chl-a tends to zero in the two size classes, respectively. The Chl-a fraction of nanoplankton (F_2) and microplankton (F_3) are calculated as $F_2 = F_{1,2} - F_1$ and $F_3 = 1 - F_{1,2}$, respectively. To derive the single set of model parameters, Eqs. (6) and (7) were fitted to *in-situ* C, $F_{1,2}$, and F_1, using the non-linear least-squares minimisation ('lmfit' package in Python). Parameter values and confidence intervals within two standard deviations are provided in Table 2, which are comparable with values from previous studies (Brewin et al., 2011, 2015, 2017).

2.4.2. SST-dependent model of Brewin et al. (2017)

By relating the parameters of the three-component model to SST, Brewin et al. (2017) proposed a SST-dependent model that estimates Chl-a for four populations of phytoplankton (i.e., picoplankton, nanoplankton, dinoflagellates, and diatoms) as a function of Chl-a and SST. To investigate the impact of temperature on the model parameters, we followed a similar approach to Brewin et al. (2017). The whole global training dataset was partitioned into lower and higher temperature waters, with the temperature threshold set at 10.5 °C (see Table 2 in Racault et al., 2012, where 10.5 °C is within the temperature range for phytoplankton growth at ± 40–50° latitudes), and model parameters were fitted separately to the two sub-datasets, as shown in Supplementary Table S2 and Figure S5. Different values of model parameters of the SST-independent model were observed for low and high temperature waters, indicating that model parameters vary with SST. Moreover, PSCs derived from two *in-situ* datasets (i.e., HPLC pigments and SFF) were further partitioned at SST = 10.5 °C, and model parameters were re-fitted to each partition. Model parameters, obtained from fitting the three-component model to the different methodologies (HPLC and SFF) at low and high temperature waters separately, showed similar changes in parameters with SST (Supplementary Figure S5), confirming consistency in the relationships between SST and size-fractionated Chl-a derived from HPLC pigments and SFF methods.

The training dataset was then sorted on the SST in the ascending order, and a running fit of Eqs. (6) and (7) was conducted as a function of SST for various bin sizes ranging from 3000 to 10,000 samples, at increments of 1000 (background lines in Fig. 2). For the running fit of each bin size, it involved sliding the bin from low to high temperature at the increment of one sample and fitting equations each time the bin slides. Relationships between SST and parameters $D_{1,2}$ and D_1 were similar to those from Brewin et al. (2017), with values increasing with increasing SST. While for $C^m_{1,2}$ and C^m_1, values derived from the global dataset exhibit more complex relationships with SST, when compared with those found by Brewin et al. (2017) in the North Atlantic region. For different bin sizes, dependencies between SST and model parameters were slightly different (Fig. 2), especially for $C^m_{1,2}$.

The relationships between parameters and SST were represented using logistic functions, as described in Brewin et al. (2017), such that,

$$C^m_{1,2} = 1 - \left\{\frac{G_a}{1 + \exp[-G_b(\mathrm{SST} - G_c)]} + G_d\right\}, \quad (8)$$

$$C^m_1 = 1 - \left\{\frac{H_a}{1 + \exp[-H_b(\mathrm{SST} - H_c)]} + H_d\right\}, \quad (9)$$

$$D_{1,2} = \frac{J_a}{1 + \exp[-J_b(\mathrm{SST} - J_c)]} + J_d, \quad (10)$$

Table 2
Parameter values for the SST-independent model and SST-dependent models in this study and in previous studies (Brewin et al., 2011, 2015, 2017). Bracketed values of results in this study refer to the 5.55 and 94.45% confidence intervals (i.e., within two standard deviations) on the distribution. Note that parameters used in this study were rounded to two decimal places, which explained why values of some parameters lie outside the confidence intervals.

Model	SST-independent model				SST-dependent model (16-parameter)			SST-dependent model (17-parameter)	
Study	Brewin et al. (2011)	Brewin et al. (2015)	Brewin et al. (2017)	This study	Model parameters	Brewin et al. (2017)	This study	Model parameters	This study
Region	Global	Global	North Atlantic	Global		North Atlantic	Global		Global
N	256	5841	2239	30579		2239	30579		30579
$C_{1,2}^m$	0.78	0.77 (0.72 – 0.84)	0.82 (0.76 – 0.88)	0.95 (0.927 – 0.968)	G_a	−1.51 (−1.57 – −1.43)	−0.56 (−0.562 – −0.549)	U_a	0.003 (0.0029 – 0.0030)
					G_b	−1.25 (−1.41 – −1.25)	−3.79 (−4.053 – −3.549)	U_b	−0.08 (−0.086 – −0.084)
					G_c	14.95 (14.87 – 15.05)	1.92 (1.888 – 1.944)	U_c	1.61 (1.610 – 1.619)
					G_d	0.25 (0.23 – 0.26)	−0.14 (−0.142 – −0.137)	/	/
					r	0.98	0.78	r	0.81
C_1^m	0.15	0.13 (0.12 – 0.14)	0.13 (0.12 – 0.13)	0.17 (0.167 – 0.174)	H_a	0.29 (0.28 – 0.30)	−0.28 (−0.279 – −0.272)	V_a	0.52 (0.521 – 0.522)
					H_b	3.05 (2.87 – 3.26)	1.13 (1.070 – 1.187)	V_b	12.71 (12.696 – 12.714)
					H_c	16.24 (16.19 – 16.29)	5.03 (4.957 – 5.103)	V_c	8.95 (8.939 – 8.966)
					H_d	0.56 (0.55 – 0.57)	0.89 (0.892 – 0.898)	V_d	0.30 (0.298 – 0.302)
					/	/	/	V_e	27.52 (27.469 – 27.579)
					/	/	/	V_f	4.61 (4.557 – 4.656)
					r	0.91	0.79	r	0.99
$D_{1,2}$	0.89	0.94 (0.93 – 0.95)	0.87 (0.86 – 0.89)	0.87 (0.868 – 0.878)	J_a	0.370 (0.367 – 0.373)	0.39 (0.390 – 0.392)	J_a	0.39 (0.390 – 0.392)
					J_b	1.13 (1.10 – 1.16)	0.33 (0.330 – 0.333)	J_b	0.33 (0.330 – 0.333)
					J_c	14.89 (14.87 – 14.91)	8.02 (8.000 – 8.047)	J_c	8.02 (8.000 – 8.047)
					J_d	0.569 (0.566 – 0.571)	0.55 (0.546 – 0.547)	J_d	0.55 (0.546 – 0.547)
					r	1.00	1.00	r	1.00
D_1	0.75	0.80 (0.78 – 0.82)	0.73 (0.71 – 0.76)	0.67 (0.658 – 0.675)	O_a	0.503 (0.501 – 0.505)	0.65 (0.647 – 0.650)	O_a	0.65 (0.647 – 0.650)
					O_b	1.33 (1.31 – 1.37)	0.22 (0.222 – 0.224)	O_b	0.22 (0.222 – 0.224)
					O_c	17.31 (17.28 – 17.32)	12.79 (12.772 – 12.800)	O_c	12.79 (12.772 – 12.800)
					O_d	0.258 (0.256 – 0.259)	0.09 (0.085 – 0.087)	O_d	0.09 (0.085 – 0.087)
					r	1.00	1.00	r	1.00

and

$$D_1 = \frac{O_a}{1 + \exp[-O_b(\mathrm{SST} - O_c)]} + O_d, \quad (11)$$

where G_a and G_d control the upper and lower bounds of $C_{1,2}^m$, G_b represents the slope of the change in $C_{1,2}^m$ with SST, and G_c is the SST mid-point of the slope between $C_{1,2}^m$ and SST. For C_1^m, $D_{1,2}$ and D_1, H_i, J_i and O_i (i = a–d) are analogous to G_i for $C_{1,2}^m$. The 16 parameters in Eqs. (8)–(11) were derived by fitting the equations to SST, $C_{1,2}^m$, C_1^m, $D_{1,2}$, and D_1. For the fits, we applied the non-linear least-squares minimisation ('lmfit' package in Python) on a running-fit bin size of 6000 samples, and the results are shown in Table 2 and Fig. 2. This model is referred to as the 16-parameter SST-dependent model henceforth. The derived parameters were relatively insensitive to bin size as illustrated in Supplementary Figure S6.

2.4.3. A new SST-dependent model with 17 parameters

The relationships between the asymptotic maximum values (i.e., $C_{1,2}^m$ and C_1^m) and SST (background lines in Figs. 2b and 2c) were found to be complex, compared to the 16-parameter model (Fig. 2b). For example, in low and high SST regions (i.e., < 5 °C, > 23 °C), the $C_{1,2}^m$ values are higher than those in the intermediate SST range, and therefore, the relationship could be represented using a quadratic polynomial function, such that,

$$C_{1,2}^m = U_a\mathrm{SST}^2 + U_b\mathrm{SST} + U_c. \quad (12)$$

Additionally, the C_1^m has a significant peak between 10 and 15 °C, a trough between 20 and 25 °C, and a potential peak over 25 °C (Fig. 2), in agreement with niche partitioning of three picoplankton groups along a temperature gradient (Flombaum et al., 2020). This relationship could be represented with a two-term Gaussian function, such that,

$$C_1^m = V_a \exp[-(\frac{\mathrm{SST} - V_b}{V_c})^2] + V_d \exp[-(\frac{\mathrm{SST} - V_e}{V_f})^2], \quad (13)$$

where parameter V_a and V_d are the height of peaks, V_b and V_e are the position of peak centres, and V_c and V_f control the width of curves. As for $D_{1,2}$ and D_1, their relationships with SST remain the same as Eqs. (10) and (11). This SST-dependent model is referred to as the 17-parameter SST-dependent model henceforth. The 17 parameters in Eqs. (10)–(13) are shown in Table 2 and illustrated in Fig. 2. Statistical tests indicate that the 17-parameter SST-dependent model explains

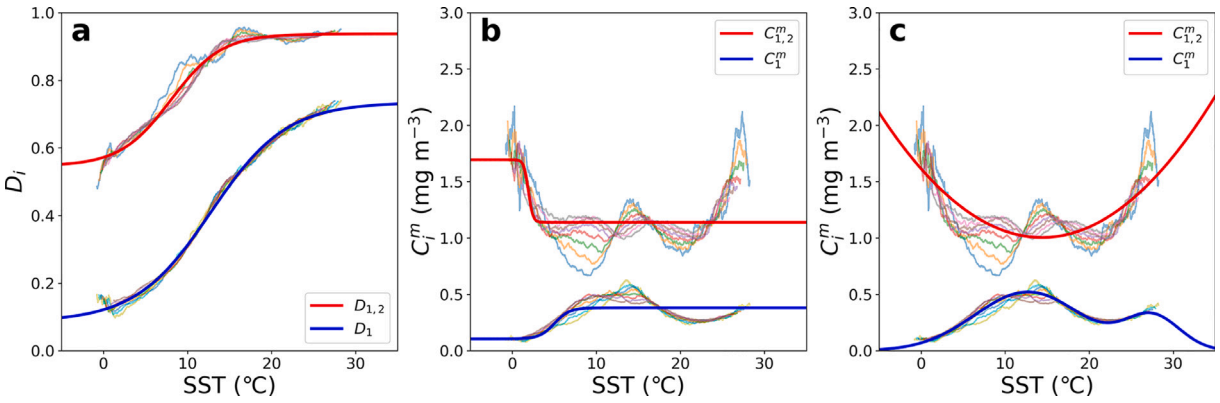

Fig. 2. Relationships between SST and $D_{1,2}$ and D_1 (a), $C_{1,2}^m$ and C_1^m from 16-parameter model (b), and $C_{1,2}^m$ and C_1^m from 17-parameter model (c). The background lines show the relationships between SST and parameters, which were derived from fits with different bin sizes from 3000 to 10,000 samples, at increments of 1000. Blue and red lines represent relationships fitted between parameters and SST using the 6000-sample running fit through non-linear least squares minimisation, with the parameter values provided in Table 2. (For interpretation of the references to colour in this figure legend, the reader is referred to the web version of this article.)

more of the variance in the asymptotic maximum values than the 16-parameter model, with higher correlations at 0.81 and 0.99 for $C_{1,2}^m$ and C_1^m, respectively.

2.5. Statistical tests

2.5.1. Model evaluation

The performance of the model was quantified using the following statistical tests: Pearson linear correlation coefficient (r), p-value (p), bias (δ), mean absolute difference (MAD, ϵ), and root mean squared difference (RMSD, ψ) between measured and modelled data. The δ, ϵ, and ψ were computed according to,

$$\delta = \frac{1}{N}\sum_{i=1}^{N}(X_i^E - X_i^M), \tag{14}$$

$$\epsilon = \frac{1}{N}\sum_{i=1}^{N}|X_i^E - X_i^M|, \tag{15}$$

and

$$\psi = [\frac{1}{N}\sum_{i=1}^{N}(X_i^E - X_i^M)^2]^{1/2}, \tag{16}$$

where X is the variable (e.g., Chl-a concentration or fraction), E and M represent estimated and measured variables, respectively, and N is the number of samples. Considering that Chl-a concentrations are distributed log-normally in the ocean (Supplementary Figure S3), statistical tests for concentrations were performed in $\log_{10}$ space, while for Chl-a fractions, statistical tests were calculated in linear space. In addition, the Akaike Information Criterion (AIC) was obtained from the non-linear least-squares minimisation ('lmfit' package in Python) and included for comparing the quality of models by quantifying the balance between the goodness of fit and simplicity. More information about the AIC statistic can be found on the following website (https://lmfit.github.io/lmfit-py/fitting.html).

2.5.2. Time-series analysis

40-year trends of SST and SST-derived model parameters were computed using linear regression, as described in Brewin et al. (2014a), such that,

$$Y = SX + I, \tag{17}$$

where Y is the monthly anomalies of SST or model parameters, calculated by subtracting the corresponding climatological monthly means over the entire period from each monthly composite on a per grid point basis, X is the time in decimal years, S is the slope of the regression, and I is the intercept. Trends (S) are shown only where correlations (r) in Eq. (17) are statistically significant ($p < 0.05$).

3. Results

3.1. Independent validation

The independent validation dataset ($N = 6011$) was used to verify and compare the performance of the three proposed models. Both SST-independent and SST-dependent models are seen to have reasonable accuracy in estimating concentrations of PSCs (Fig. 3), with r over 0.920, 0.858, 0.843, and 0.582 for C_3, $C_{1,2}$, C_2, and C_1, respectively. The overall accuracy improves using the SST-dependent models, with higher correlation coefficients, lower bias, MAD, and RMSD for all the size classes (Fig. 3). Significant improvements are observed for picoplankton in the SST-dependent models, with r increasing from 0.582 to 0.729 (0.689) and ψ decreasing from 0.400 to 0.329 (0.348) for the 16-parameter model (17-parameter model). The AIC of SST-dependent models are found to be lower than the SST-independent model (Supplementary Table S3), indicating that the introduction of more environmental variables (i.e., SST) and model parameters results in higher model performance. Statistical tests on the Chl-a fractions of PSCs also suggest that SST-dependent models perform better than the SST-independent model, and the performances of the proposed SST-dependent models in this study are found have better statistical performances than those presented in previous studies (Hirata et al., 2011; Brewin et al., 2015, 2017; Liu et al., 2021, see Supplementary Table S4), acknowledging that some of these models have not been developed for global application.

Compared with *in-situ* measurements, histograms of the density distribution of Chl-a show that all three models have comparable capability in estimating C_3 (Fig. 3d). However, densities of smaller size groups, i.e., $C_{1,2}$ and C_1, derived from the SST-independent model reach their maximum at 1.0 and 0.2 mg m^{-3}, respectively, and deviate from the density distribution of *in-situ* Chl-a measurements, as expected from the constrained static asymptotes in Figs. 3a2 and 3a4 (dashed purple lines). By comparison, validation results indicate that the SST-dependent models have a better capability in capturing the variability of $C_{1,2}$ and C_1 at high concentrations (Figs. 3b2, 3b4, 3c2, and 3c4), in better agreement with the density distributions of the *in-situ* Chl-a measurements (Fig. 3g). In general, 16-parameter and 17-parameter SST-dependent models have broadly similar performances in estimating both Chl-a concentration and fractions for the three size classes (Fig. 3 and Supplementary Table S4). The 16-parameter model with logistic functions shows slightly better accuracy for all the size classes, while the 17-parameter model, with the additional polynomial and Gaussian functions, has advantages in estimating picoplankton at higher concentrations, which can be seen from the density comparison of Chl-a and from the bias approaching zero (Figs. 3c4, 3g).

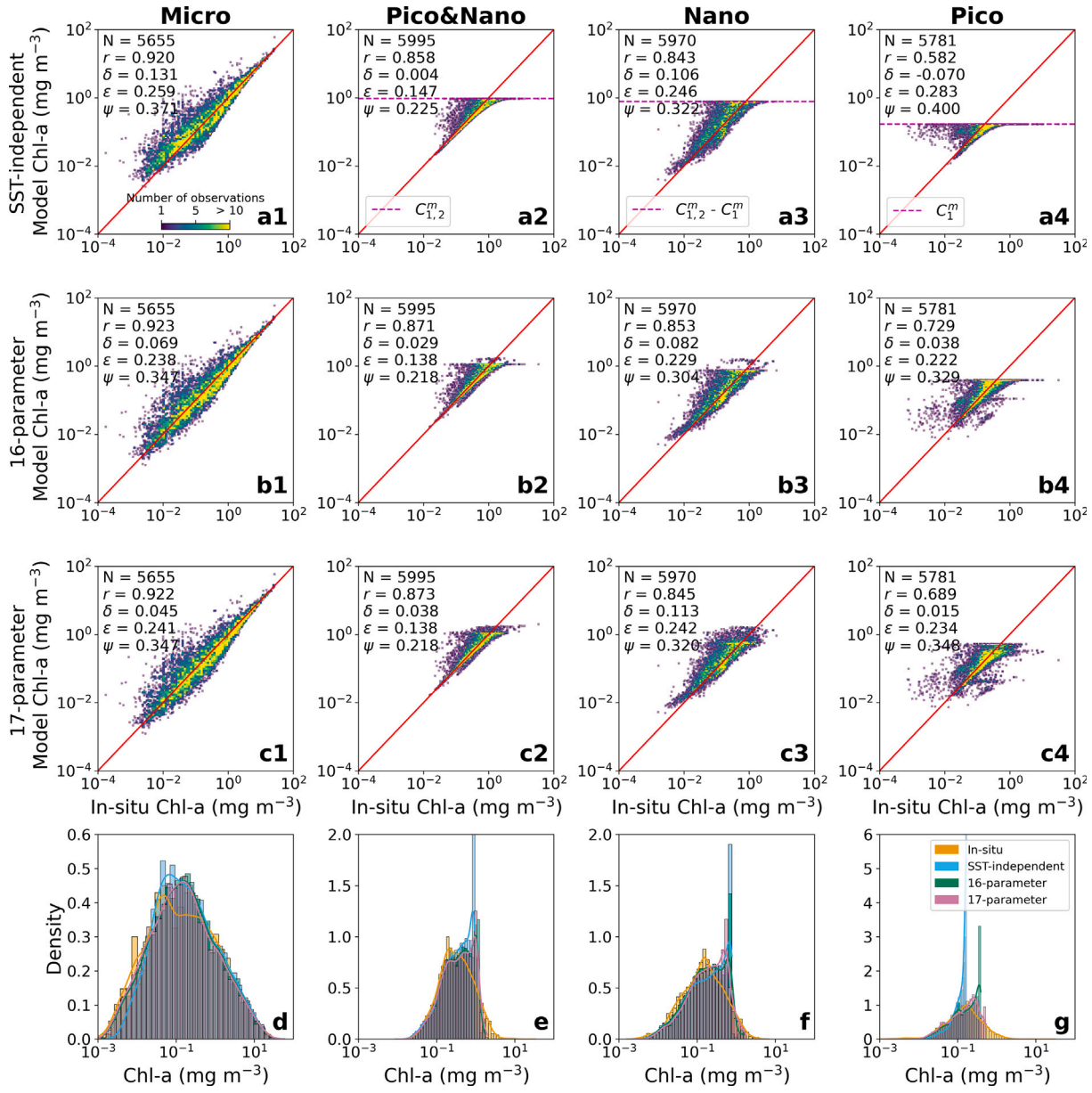

Fig. 3. Independent validation between *in-situ* and modelled size-fractionated chlorophyll-a concentrations derived from the SST-independent model (a1–a4), 16-parameter SST-dependent model (b1–b4), and 17-parameter SST-dependent model (c1–c4), with statistical tests shown in each subplot. Histograms of density between *in-situ* measurements and modelled results (d–g) from the three rows above. Dashed purple lines in a2–a4 represent the maximum attainable concentrations for different size classes when using the SST-independent model. (For interpretation of the references to colour in this figure legend, the reader is referred to the web version of this article.)

To investigate which of the SST-dependent model parameters have the largest impact on model retrievals, we fixed $C^m_{1,2}$ and C^m_1 at 1.22 and 0.32, respectively (i.e., mean value of the 6000-sample running fit), leading to an 8-parameter SST-dependent model (i.e., Eqs. (10) and (11) for $D_{1,2}$ and D_1), and re-ran the validation, as shown in Supplementary Table S4. Statistical tests indicate that by fixing the asymptotic maximum values, the 8-parameter model performed better than the SST-independent model, and exhibits similar (albeit slightly poorer) accuracy than 16-parameter and 17-parameter models. Results imply that the dependency on SST of $D_{1,2}$ and D_1 is more important than that of $C^m_{1,2}$ and C^m_1 in the SST-dependent models.

3.2. SST-dependent model parameter trends from 1981 to 2021

Before investigating the impact of changes in SST on SST-dependent model parameters, a comparison of SST trends was conducted between monthly OISST and SST-CCI products over the same time frame (i.e., from December 1981 to December 2017), as shown in Supplementary Figure S7. A similar geographical distribution of trends are observed for both datasets globally, with only a few areas showing slight differences (e.g., polar areas), suggesting consistency between monthly OISST and SST-CCI products. Considering the longer time coverage for both daily and monthly products, and that it was used for model training and validation, we used OISST monthly datasets hereafter for analysis of trends in model parameters.

Fig. 4 shows the global map of the 40-year trend (i.e., from December 1981 to November 2021) in monthly OISST data. Significant increasing trends ($p < 0.05$) are observed in most of the global ocean (~ 71%), particularly along the Gulf Stream in the North Atlantic, the Kuroshio in the North Pacific, the Brazil Current in the South Atlantic, and the East Australia Current in the South Pacific. In the western equatorial Pacific Ocean, values of the SST trend are not as significant as those in other areas (light grey pixels). The ~ 12% of the global ocean that was found to have significant decreasing trends, included

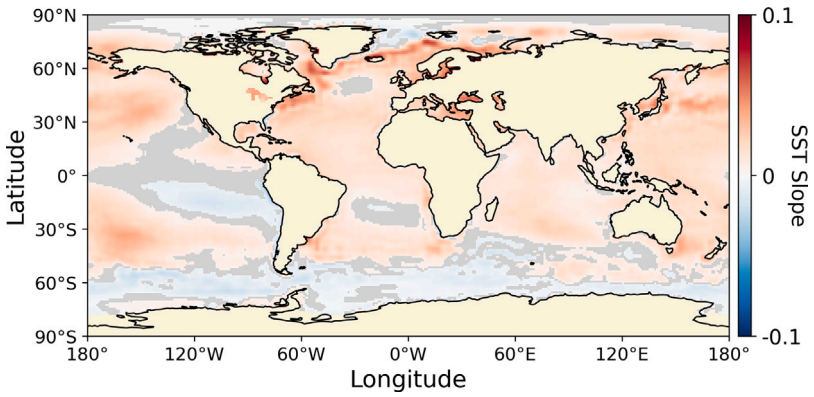

Fig. 4. Global map of the trends in monthly OISST SST data from December 1981 to November 2021. Only significant trends (slope) are shown (where $p < 0.05$). Light yellow pixels represent land or invalid data, and light grey pixels represent areas with insignificant trends. (For interpretation of the references to colour in this figure legend, the reader is referred to the web version of this article.)

the Greenland Sea in sub-polar North Atlantic, the Peru Current region in the South Pacific, and large parts of the Southern Ocean. These SST trends in Fig. 4 are in good agreement with those from a daily-based global climate SST analysis (European Union-Copernicus Marine Service, 2019).

Using monthly OISST data as input to the 16-parameter and 17-parameter SST-dependent models allowed us to reconstruct 40-year trends in model parameters ($C^m_{1,2}$, C^m_1, $D_{1,2}$, and D_1), as shown in Fig. 5. Not surprisingly, considering the positive relationships shown in Fig. 2a, the geographical patterns in the trends of $D_{1,2}$ and D_1 are similar to that of SST. The increasing (decreasing) SST leads to higher (lower) $D_{1,2}$ and D_1. The trends in $C^m_{1,2}$ and C^m_1 derived from 16-parameter model (Figs. 5c and 5d) have smaller areas with significant positive and negative slopes globally, at ~ 7% and ~ 12% respectively, which reflect the fact that relationships between these parameters and SST are fixed at temperatures greater than about 5 °C and 10 °C in the 16-parameter model (Fig. 2b). As a result, the majority of significant trends in $C^m_{1,2}$ and C^m_1 using the 16-parameter model are observed in polar regions (Figs. 5c and 5d). In agreement with the 16-parameter model, the 17-parameter SST-dependent model produces similar trends in $C^m_{1,2}$ and C^m_1 in these polar regions. Here, the $C^m_{1,2}$ trends are in general the opposite to those of C^m_1. At lower latitudes, the 17-parameter SST-dependent model yields more areas with significant positive and negative trends in $C^m_{1,2}$ and C^m_1 than the 16-parameter model (~ 81% and ~ 70% respectively at global scale, Figs. 5e and 5f). In these middle and low latitude regions, $C^m_{1,2}$ trends in the 17-parameter SST-dependent model are similar to those of SST, given the positive relationship between $C^m_{1,2}$ and SST above 10 °C (Fig. 2c). The trends in C^m_1 in these middle and low latitude regions are more intricate (Fig. 5f), as anticipated from the non-monotonic relationship between C^m_1 and SST above 10 °C in the 17-parameter model (Fig. 2c).

To illustrate potential changes in phytoplankton size structure over the 40-year period, caused solely by SST-dependent changes in model parameters and independent of any change in total Chl-a, we computed global maps of model parameters in March 1984 and March 2020 using OISST data, then computed global maps of the fractions of each size class using the same OC-CCI Chl-a March climatology as input. We selected 1984 and 2020 (rather than 1981 and 2021) to minimise the influence of El Niño events (values of MEI.v2 were close to zero at both FM (February-March) and MA (March-April) in 1984 and 2020, https://psl.noaa.gov/enso/mei/). Fig. 6 illustrates the differences between the two periods (i.e., March 1984 and March 2020) in the fractions of the three size classes. Since the same Chl-a climatology (i.e., March) was used in the analysis, simulated differences over the 37 years are caused solely by SST, and assume no change in total Chl-a. In general, differences in fractions are more evident at higher latitudes than lower latitudes. Microplankton fractions derived from the 16-parameter model declined to the north/south of ± 30° latitudes, such as the 40° latitude in North Pacific Ocean, and some increases were observed in the northern North Atlantic Ocean and Southern Ocean, while there was no evident difference around the equator. Nanoplankton showed an overall decrease in low and middle latitude regions (around ± 30° latitudes), with the exception of an increasing trend in the East Pacific Ocean. Picoplankton showed the most noticeable differences globally, which were opposite to those of microplankton. The differences between 16-parameter and 17-parameter models are mainly in the variations of nanoplankton and picoplankton at lower latitudes, with larger areas of increases (decreases) of nanoplankton (picoplankton) fractions observed in the equatorial Indian and Pacific oceans using the 17-parameter model. For regional studies, we recommend evaluating the 16-parameter and 17-parameter models using an independent regional validation dataset, prior to selecting an approach.

4. Discussion

4.1. Selection of the three-component model

There is a wide range of models that relate Chl-a to PSCs, including statistical (Uitz et al., 2006), empirical (Hirata et al., 2011; Moore and Brown, 2020), and conceptual methods (Sathyendranath et al., 2001; Devred et al., 2006, 2011; Brewin et al., 2010, 2015, 2017). The method of Uitz et al. (2006) is based on a statistical analysis of a broad range of trophic conditions partitioned into stratified and mixed waters, using information on Chl-a, mixed-layer depth and euphotic depth. Other methods are based solely on Chl-a; for example, the method of Hirata et al. (2011) is purely empirical. These statistical and empirical models were developed from data collected in the past, which may not reflect a future ocean under climate change. The three-component model of Brewin et al. (2010) relates Chl-a to PSCs using an underlying conceptual model (Sathyendranath et al., 2001). It is constrained in its flexibility to fit the data with this underlying concept, unlike the methods of Uitz et al. (2006) and Hirata et al. (2011), but it is a parsimonious model which requires only four parameters ($C^m_{1,2}$, C^m_1, $D_{1,2}$, and D_1) that are interpretable (Sathyendranath et al., 2001; Devred et al., 2006; Brewin et al., 2011).

Of these available models, the three-component model was selected in this study for two reasons. Firstly, it has been extensively evaluated and validated (both directly and conceptually) in a wide range of environments, using large amounts of *in-situ* data and numerical model simulations (see Supplementary Table S5 that list 69 studies using the model). Consistent with the assumptions of the three-component model, field observations and model simulations have shown that as the total phytoplankton biomass increases, smaller size classes reach the maximum biomass asymptotically, allowing larger size classes to thrive (e.g., Gin et al., 2000; Ward et al., 2012). Secondly, the three-component model is conceptual, which is more desirable for developing

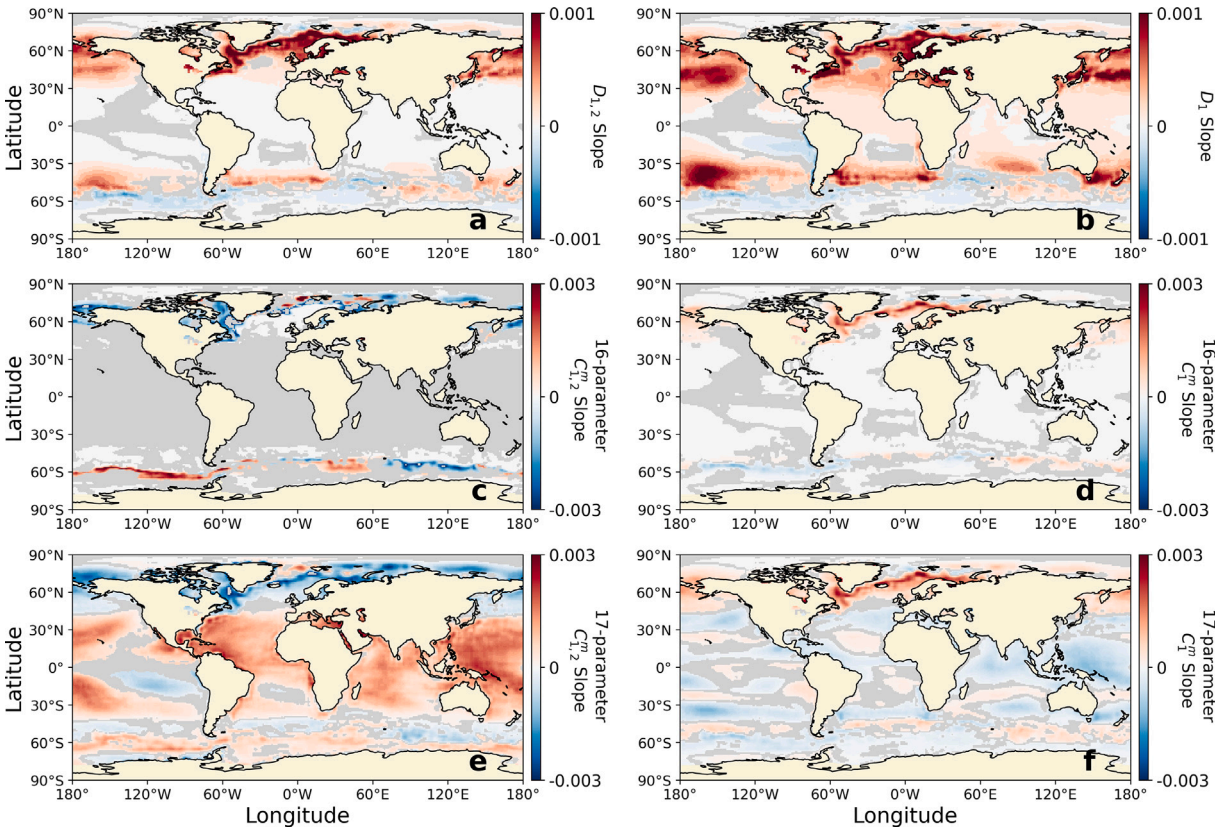

Fig. 5. Global maps of the trends in monthly SST-derived model parameters, $D_{1,2}$ and D_1 (a, b), $C^m_{1,2}$ and C^m_1 from 16-parameter model (c, d), and $C^m_{1,2}$ and C^m_1 from 17-parameter model (e, f), from December 1981 to November 2021. Only significant trends (slope) are shown (where $p < 0.05$). Light yellow pixels represent land or invalid data, and light grey pixels represent areas with insignificant trends. (For interpretation of the references to colour in this figure legend, the reader is referred to the web version of this article.)

ocean-colour algorithms in climate change studies (Sathyendranath et al., 2017), when compared with empirical approaches. Parameters of the model, such as the asymptotic maxima ($C^m_{1,2}$ and C^m_1), have direct relevance to ecosystem studies and ecology, which are impacted by bottom-up processes, such as changes in the growth rates of different size classes from changing nutrient input, temperature or underwater light (Raimbault et al., 1988; Sathyendranath and Platt, 2007; Marañón et al., 2012), and by top-down processes, such as size-dependent grazer control (Goericke, 2002).

4.2. Relationships between model parameters and SST

Relating the parameters of the three-component model to environmental variables extends the approach from a purely abundance-based method to an ecological one (Brewin et al., 2015, 2017, 2019b). Relationships between model parameters and SST (Supplementary Figure S5) are in broad agreement with those proposed by Ward (2015, see their Figure 2), showing a general decline in picoplankton and an increase in micro- and nanoplankton with decreasing temperature. The relationship between temperature and model parameters could be direct, for example, through a direct metabolic response of phytoplankton to temperature (López-Urrutia and Morán, 2015), and/or indirect, for example, due to changes in nutrients (e.g., upwelling) or light availability that correlate with temperature (Finkel et al., 2009; Marañón et al., 2012, 2015). At high latitudes, decreasing SST is often associated with enhanced surface mixing and/or weakening of solar radiation. Larger cells (e.g. diatoms) are known to thrive in such turbulent waters (Marañón et al., 2012; Xi et al., 2021), perhaps explaining the shifts to larger cells in the model with decreasing SST. Increases in $D_{1,2}$ and D_1 over the last 40 years at high latitudes (Fig. 5) are consistent with increases in smaller phytoplankton in some polar regions (Fig. 6), supporting observations of shifts from larger- to smaller-sized phytoplankton in the Arctic Ocean (Ardyna and Arrigo, 2020, and references therein) and Northern Antarctic Peninsula (Ferreira et al., 2020). This poleward expansion of smaller size classes under global warming could be explained by enhanced stratification, a reduction in nutrient supply, and an increase in light availability (Li et al., 2009; Marinov et al., 2010; Morán et al., 2010; Siegel et al., 2013). On the contrary, in some regions of the Antarctic, shifts in phytoplankton size towards large cells are also evident (Fig. 6), in agreement with a previous study in the southern region of Western Antarctic Peninsula (Montes-Hugo et al., 2009). The increase of larger size classes are likely caused by nutrient-rich water associated with stronger winds and glacier retreat. These contrasting effects of environmental drivers on phytoplankton dynamics indicate the complexity of polar biogeography. In addition, changes in SST may also impact the taxonomic composition within certain size classes. For example, in coastal waters of the Red Sea, Brewin et al. (2019b) found *Synechococcus* to be positively correlated with temperature and picoeukaryotes negatively correlated. These changes were subsequently linked to temperature changes in C^m_1 using the three-component model. Over large scales, temperature is known to be related to the taxonomic composition of picoplankton (Flombaum et al., 2013; Lange et al., 2018). Flombaum et al. (2020) observed clear niche partitioning along the gradient of temperature among picoeukaryotes, *Synechococcus*, and *Prochlorococcus* in global ocean, where the abundances of picoeukaryotes and *Synechococcus* peak at 8.5 °C and 10 °C, while *Prochlorococcus* dominates at high temperature (> 13 °C), and this taxonomic composition is expected to be impacted by climate change (Flombaum and Martiny, 2021).

There are differences in the relationships between model parameters and SST reported here and those from previous regional studies (Brewin et al., 2017, 2019b; Sun et al., 2019; Liu et al., 2021; Turner et al., 2021). These are likely caused by regional differences in *in-situ* datasets

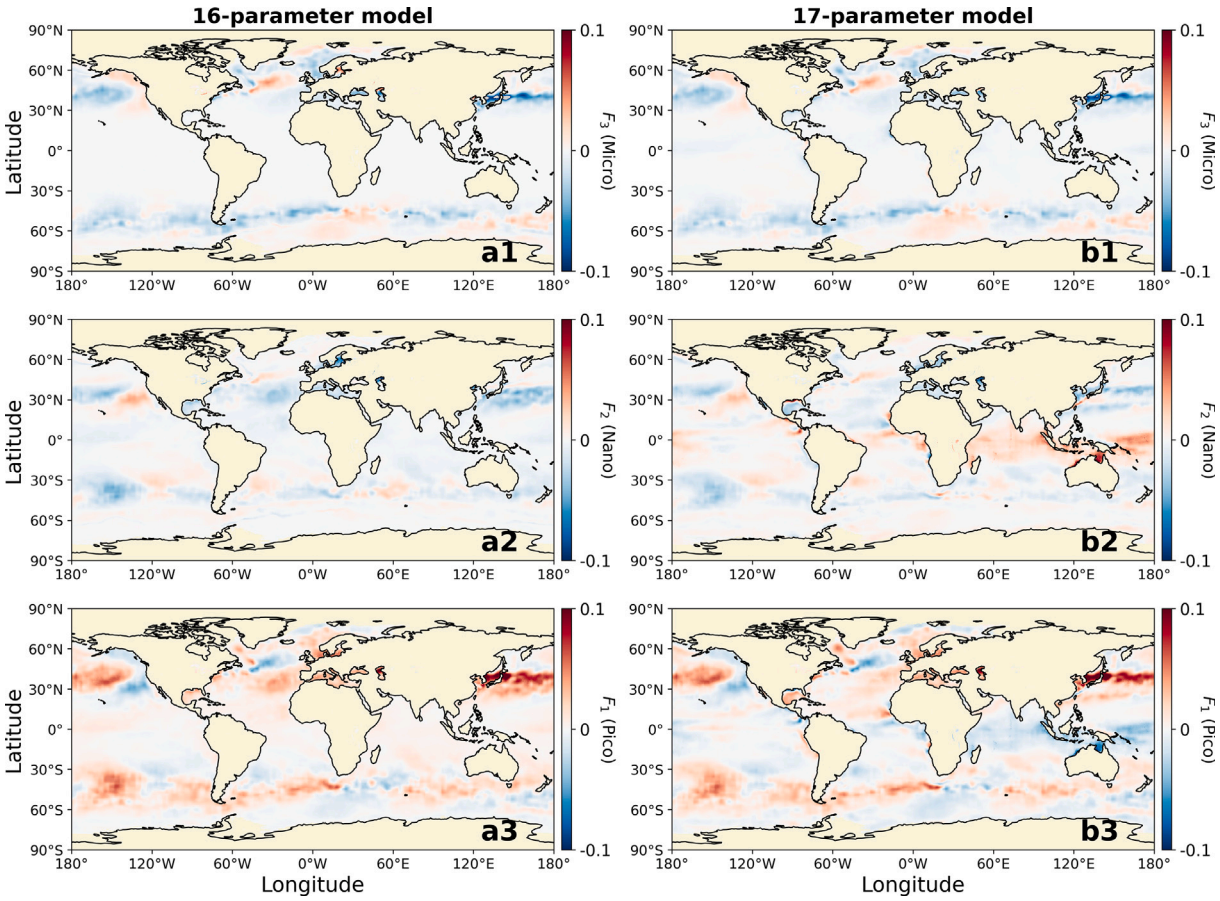

Fig. 6. Global maps of the fractional differences of phytoplankton size classes in March between 1984 and 2020, where fractions of concentration were derived from monthly OISST SST data and monthly OC-CCI Chl-a climatology data using the 16-parameter model (a1–a3) and 17-parameter model (b1–b3), respectively. Light yellow pixels represent land or invalid data. (For interpretation of the references to colour in this figure legend, the reader is referred to the web version of this article.)

used for tuning the SST-dependent model. Here, we compiled a huge amount data in the global ocean, including a large number of samples from low-temperature waters at high latitudes (Fig. 1 and Supplementary Figure S3), and obtained relationships between model parameters and temperature covering a more comprehensive range in SST (−0.12 to 27.14 °C under the condition of 6000 bin size in the running fit). Although the SST-dependent model has proven successful in capturing relationships between total and size-fractionated Chl-a, large variations in $C_{1,2}^{m}$ and C_{1}^{m} are still seen at some temperature ranges (e.g. 2–10 °C, see background lines in Fig. 2), which may relate to the relatively small number of samples in this SST range (Supplementary Figure S3). Considering these relationships were derived from the data collected in the past, there is a strong requirement to keep revisiting these relationships as new datasets are collected, since the relationships between model parameters and SST may themselves be subject to future climatic change.

4.3. Applications of the model to satellite data

Up to now, abundance-based PSCs models have been implemented extensively in global and regional waters by using satellite products of Chl-a as input (e.g., Brewin et al., 2010; Hirata et al., 2011; Ward, 2015). Even though these models have proven useful for obtaining spatial and temporal distributions in PSCs, there is an inconsistency in this type of application. For example, some empirical satellite Chl-a retrieval algorithms, such as the successful and well-tested OC4 algorithm (O'Reilly et al., 1998), have been shown to implicitly assume shifts in phytoplankton size structure with total Chl-a (Dierssen, 2010; Brewin et al., 2014b; Sathyendranath et al., 2017), while other algorithms do not (e.g., GSM, Garver and Siegel, 1997; Maritorena et al., 2002). These implicit assumptions may be at odds with the parameterisation of the PSCs models. For example, at low Chl-a values, the OC4 algorithm has been shown to lie close to a theoretical picoplankton-tuned ocean-colour model (see Figure 4.7 in Brewin et al., 2014b), which agrees with our SST-dependent model for high temperature waters. However, this is in disagreement with our SST-dependent model in low temperature waters at low Chl-a values, where larger cells (> 2 μm) become more prevalent, as shown in Supplementary Figure S5. We are now in a position to take these abundance-based algorithms one step further by explicitly integrating them into a model of ocean colour (e.g., see Brewin et al., 2015), incorporating ecological variation as indicated through changes in SST. Such an approach has the potential to improve the accuracy in satellite Chl-a estimates and ensure compatibility between estimates of Chl-a and those of the PSCs. These next steps will be described in subsequent papers in this series.

Including ecology in a model of ocean colour may help reconcile differences observed between regional and global empirical satellite Chl-a algorithms. For example, standard Chl-a retrieval algorithms are known to underestimate Chl-a in the Southern Ocean (Dierssen and Smith, 2000; Korb et al., 2004; Szeto et al., 2011). This has been attributed to different relationships between bio-optical properties and Chl-a (Mitchell and Holm-Hansen, 1991; Dierssen et al., 2000; Reynolds et al., 2001). Higher contributions of microplankton have been observed in the Southern Ocean for the same Chl-a concentration when compared to other regions, resulting in a strong package effect and a flattening of the chlorophyll-specific absorption coefficient (Bracher and Tilzer, 2001; Robinson et al., 2021). The shift towards larger cells with decreasing temperature is captured in our ecological model, and

when coupled to the optical properties of the three size classes, it may have the capability to account for such regional variations (e.g., see Brewin et al., 2019a, in the North Atlantic).

4.4. Implications of climate change for phytoplankton

The ocean has absorbed about 93% of the excess heat energy and around 25% of excess atmospheric CO_2 caused by anthropogenic climate change (Rhein et al., 2013; Friedlingstein et al., 2021). Understanding how this is impacting the ocean has become a key issue worldwide. Among the physical attributes, SST is an essential climate variable, making the monitoring and quantification of SST trends fundamental for climate studies (Merchant et al., 2019). Long-term global satellite SST datasets show that the majority of the ocean has been experiencing strong warming trends, particularly along the northern edge of Northern Hemisphere western boundary currents, but with smaller areas in the eastern tropical Pacific and high latitudes showing a relatively weak cooling trend (Wu et al., 2012; Bulgin et al., 2020; Johnson and Lyman, 2020). Our observations are in accordance with these findings (see Fig. 4). Many studies have demonstrated that phytoplankton are susceptible to ocean warming, with increasing SST at low latitudes causing enhanced stratification and reduced total phytoplankton biomass (Behrenfeld et al., 2006; Boyce et al., 2010), alterations in the timing of phytoplankton blooms (Kahru et al., 2010; Gittings et al., 2018), shifts in the community structure towards smaller sized cells (Li et al., 2009; Morán et al., 2010; Mouw et al., 2019), and a different taxonomic composition (Anderson et al., 2021). In agreement with some of these studies, we show evidence of an SST-dependent shift towards smaller-celled phytoplankton (picoplankton), particularly in high-latitude regions (see Fig. 6), independent of any change in total Chl-a (noting that Fig. 6 does not reflect actual differences in fractions of PSCs, since it does not include changes in total Chl-a). The SST-dependent models can extend our understanding of phytoplankton size structure beyond the lifespan of the existing continuous ocean-colour record (e.g., 1984 in Fig. 6), allowing for the explanation of observed variations of phytoplankton dynamics over a longer time series. Nonetheless, quantifying actual shifts in size structure over the period when satellite ocean-colour data are available would require disentangling the influence of trends in size structure, Chl-a, and other optically-active substances (e.g. CDOM and NAP), on trends in remote-sensing reflectance.

As a common proxy of phytoplankton biomass, Chl-a concentration is recognised as an Essential Climate Variable (GCOS, 2011), and also a key input to many ecological indicators, such as phytoplankton phenology, primary production, phytoplankton functional types, and phytoplankton size structure (Platt and Sathyendranath, 2008; Racault et al., 2012; Kulk et al., 2020; Tilstone et al., 2023). Including SST, another fundamental indicator of the climate system, into models of ocean colour, may result in better performance in satellite Chl-a retrievals (Gholizadeh and Robeson, 2016), and advance our understanding of how these indicators are responding to climate change and the ecological and biogeochemical consequences. Nonetheless, Chl-a can change independently of any change in phytoplankton carbon biomass in response to changes in temperature, light and nutrient supply (e.g., photoacclimation, Behrenfeld, 2014; Jackson et al., 2017; Sathyendranath et al., 2020; Brewin et al., 2022). Understanding how climate change is impacting the carbon to chlorophyll ratio is required to monitor trends in phytoplankton carbon biomass (Siegel et al., 2013; Brewin et al., 2021). This could be addressed through the use of photoaclimation models (e.g., Jackson et al., 2017; Sathyendranath et al., 2020) or the relationships between Chl-a and particle backscattering (e.g. Behrenfeld et al., 2005).

5. Summary

In this study, we created the largest (to our knowledge) global surface ($\leq$ 20 m depth) *in-situ* dataset of total and size-fractionated Chl-a from 1991 to 2021 (N = 36,590), by mining datasets from available sources and matching data to concurrent SST data from daily OISST. The dataset included two independent *in-situ* methods (i.e., HPLC and SFF) for deriving size-fractionated Chl-a. When the three-component model of Brewin et al. (2010) was fitted to these datasets separately at high and low SST waters, consistent patterns in model parameters were observed for both cases. HPLC and SFF datasets were then merged and split into training and validation datasets (i.e., based on time period, pre and post 2016), with 30,579 and 6011 samples, respectively. The three-component model was fitted to the training dataset and the derived model parameters were comparable with those from previous studies. Similarly, by introducing the dependence of model parameters on SST, the three-component model was found to significantly improve in performance when tested on the independent validation dataset, with higher correlation, and lower bias, MAD and RMSD, for the three phytoplankton size classes.

Logistic functions used to relate model parameters to SST (Brewin et al., 2017) worked well for two parameters, that represent the fractions of combined pico- and nanoplankton, and picoplankton as Chl-a tends to zero ($D_{1,2}$ and D_1). However, more complicated relationships between SST and the other two parameters ($C^m_{1,2}$ and C^m_1), that represent the maximum Chl-a concentration of their respective size classes, were observed in the global ocean. In addition to the re-tuning of logistic functions, we also proposed new polynomial and Gaussian functions that relate $C^m_{1,2}$ and C^m_1 to SST respectively, with a significant improvement in their correlations. Trends in monthly satellite SST data indicate that warming is occurring in most parts of ocean over the last 40 years. Application of these models to the SST record showed significant trends in the parameters of the three-component model over the past 40 years under climate change. Even by assuming no change in Chl-a over this period, the global increasing SST trend suggests an average shift in phytoplankton size structure towards smaller celled phytoplankton (picoplankton), but there are regional deviations from this trend.

Considering the potential for ambiguity in ocean-colour data, our results have profound implications for developing ocean-colour Chl-a algorithms that are robust to the effects of climate change, and for creating long-term data records of Chl-a concentration. Our results emphasise the importance of considering the impact of climate change on phytoplankton ecology when developing ocean-colour algorithms, which will be investigated in subsequent contributions to this series of papers.

CRediT authorship contribution statement

Xuerong Sun: Methodology, Software, Validation, Formal analysis, Investigation, Data curation, Writing – Original draft, Writing – review & editing, Visualization. **Robert J.W. Brewin:** Conceptualization, Methodology, Software, Investigation, Writing – original draft, Writing – review & editing, Supervision, Project administration, Funding acquisition. **Shubha Sathyendranath:** Investigation, Writing – review & editing. **Giorgio Dall'Olmo:** Investigation, Writing – review & editing. **Ruth Airs:** Investigation, Writing – review & editing. **Ray Barlow:** Investigation, Writing – review & editing. **Astrid Bracher:** Investigation, Writing – review & editing. **Vanda Brotas:** Investigation, Writing – review & editing. **Malika Kheireddine:** Investigation, Writing – review & editing. **Tarron Lamont:** Investigation, Writing – review & editing. **Emilio Marañón:** Investigation, Writing – review & editing. **Xosé Anxelu G. Morán:** Investigation, Writing – review & editing. **Dionysios E. Raitsos:** Investigation, Writing – review & editing. **Fang Shen:** Investigation, Writing – review & editing. **Gavin H. Tilstone:** Investigation, Writing – review & editing.

Declaration of competing interest

The authors declare that they have no known competing financial interests or personal relationships that could have appeared to influence the work reported in this paper.

Data availability

Data will be made available on request.

Acknowledgements

This work is supported primarily by a UKRI Future Leader Fellowship (MR/V022792/1). Additional supports from the UK National Centre for Earth Observation (NCEO), the Simons Foundation Project Collaboration on Computational Biogeochemical Modeling of Marine Ecosystems (CBIOMES, 549947, Shubha Sathyendranath), and Royal Society International Exchanges 2021 Cost Share (NSFC) grant (IEC\NSFC\211058) are acknowledged. Astrid Bracher and Vanda Brotas are funded by the European Union's Horizon 2020 Research and Innovation Programme (N810139): Project Portugal Twinning for Innovation and Excellence in Marine Science and Earth Observation (PORTWIMS). Astrid Bracher is also funded by the ESA 656 S5P+Innovation Theme 7 Ocean Colour (S5POC) project (No. 400012-7533/19/I-NS). The AWI *in-situ* data are supported by the Helmholtz Infrastructure Initiative FRAM. Tarron Lamont and Ray Barlow acknowledge funding, logistical, and administrative support from the South African National Department of Forestry, Fisheries and the Environment (DFFE), Bayworld Centre for Research and Education (BCRE), and the South African National Research Foundation (NRF grants: 129229 and 132073). Fang Shen is funded by National Natural Science Foundation of China (No. 42076187 and No. 41771378) for the sampling of *in-situ* data in eastern China seas. The Atlantic Meridional Transect (AMT) is funded by the UK Natural Environment Research Council (NERC) through its National Capability Long-term Single Centre Science Programme, Climate Linked Atlantic Sector Science (grant number NE/R015953/1) to Plymouth Marine Laboratory. This work contributes to the international IMBeR project and is contribution number 386 of the AMT programme. The authors would like to acknowledge all the contributors who have shared *in-situ* data to the public domains, including the Western Channel Observatory, TARA Ocean, Rothera Research Station, NASA SeaBASS, ADON, Government of Canada, DATAONE, BCODMO, EDI Data Portal, PANGAEA, and BODC, and all the scientists and crew who were involved in the collection of *in-situ* data are sincerely appreciated. We thank NOAA for providing daily and monthly OISST (version 2) SST data; ESA for providing monthly SST-CCI (version 2.1) SST data; ESA for providing monthly OC-CCI (version 5.0) Chl-a climatology data; GEBCO for providing bathymetric data (GEBCO2021 Grid). The authors also thank Hongyan Xi for providing comments and suggestions on the early version of the manuscript.

Appendix A

See Table A.1

Table A.1
Definitions of the abbreviations and symbols used in this manuscript.

Abbreviation and Symbol	Definition	Unit ('\' indicates an abbreviation)
CDOM	Coloured dissolved organic matter	\
Chl-a	Chlorophyll-a concentration	mg m^{-3}
HPLC	High performance liquid chromatography	\
NAP	Non-algal particles	\
OC-CCI	Ocean Colour Climate Change Initiative	\
OISST	Optimal Interpolation Sea Surface Temperature	\
PSCs	Phytoplankton size classes	\
SFF	Size-fractionated fluorometric	\
SST	Sea surface temperature	°C
SST-CCI	Sea Surface Temperature Climate Change Initiative	\
C	*In-situ* Chl-a concentration	mg m^{-3}
C_1, C_2, C_3, $C_{1,2}$	Concentration of picoplankton, nanoplankton, microplankton, and combined pico- and nanoplankton	mg m^{-3}
$C^m_{1,2}$, C^m_1	Asymptotic maximum values for combined pico- and nanoplankton and picoplankton	mg m^{-3}
C_w	Total chlorophyll-a concentration estimated from the weighted sum of seven diagnostic pigments	mg m^{-3}
$D_{1,2}$, D_1	Fraction of Chl-a as total Chl-a tends to zero for combined pico- and nanoplankton and picoplankton	dimensionless
F_1, F_2, F_3, $F_{1,2}$	Fraction of picoplankton, nanoplankton, microplankton, and combined pico- and nanoplankton	dimensionless
G_a, G_b, G_c, G_d	Parameters for $C^m_{1,2}$ in 16-parameter model, where G_a and G_d control the upper and lower bounds, G_b represents the slope of the change, G_c is the SST mid-point of slope	mg m^{-3}, $°C^{-1}$, °C, mg m^{-3}
H_a, H_b, H_c, H_d	Parameters for C^m_1 in 16-parameter model, same as $G_a - G_d$	mg m^{-3}, $°C^{-1}$, °C, mg m^{-3}
J_a, J_b, J_c, J_d	Parameters for $D_{1,2}$ in 16-parameter model, same as $G_a - G_d$	dimensionless, $°C^{-1}$, °C, dimensionless
O_a, O_b, O_c, O_d	Parameters for D_1 in 16-parameter model, same as $G_a - G_d$	dimensionless, $°C^{-1}$, °C, dimensionless
p	p-value	dimensionless
P	Diagnostic pigments in diagnostic pigment analyse	mg m^{-3}
$P_{1,n}$	Part of the fucoxanthin pigment in the nanoplankton pool	mg m^{-3}
q	Coefficients of pigments in diagnostic pigment analyse	dimensionless
r	Pearson linear correlation coefficient	dimensionless
U_a, U_b, U_c	Parameters for $C^m_{1,2}$ in 17-parameter model	mg m^{-3} $°C^{-2}$, mg m^{-3} $°C^{-1}$, mg m^{-3}
V_a, V_b, V_c, V_d, V_e, V_f	Parameters for C^m_1 in 17-parameter model, V_a and V_d are the height of peaks, V_b and V_e are the positions of peak centres, and V_c and V_f control the width of the curve	mg m^{-3}, °C, °C, mg m^{-3}, °C, °C
W	Weights of pigments in diagnostic pigment analyse	dimensionless*
δ	Bias	dimensionless*
ϵ	MAD, mean absolute difference	dimensionless*
ψ	RMSD, root mean squared difference	dimensionless*

*The unit depends on the input.

Appendix B. Supplementary data

Supplementary material related to this article can be found online at https://doi.org/10.1016/j.rse.2022.113415.

References

Aiken, J., Pradhan, Y., Barlow, R., Lavender, S., Poulton, A., Holligan, P., Hardman-Mountford, N., 2009. Phytoplankton pigments and functional types in the Atlantic Ocean: A decadal assessment, 1995–2005. Deep Sea Res. Part II 56 (15), 899–917. http://dx.doi.org/10.1016/j.dsr2.2008.09.017.

Alvain, S., Moulin, C., Dandonneau, Y., Bréon, F., 2005. Remote sensing of phytoplankton groups in case 1 waters from global SeaWiFS imagery. Deep Sea Res. Part I 52 (11), 1989–2004. http://dx.doi.org/10.1016/j.dsr.2005.06.015.

Anderson, S.I., Barton, A.D., Clayton, S., Dutkiewicz, S., Rynearson, T.A., 2021. Marine phytoplankton functional types exhibit diverse responses to thermal change. Nat. Commun. 12 (1), http://dx.doi.org/10.1038/s41467-021-26651-8.

Ardyna, M., Arrigo, K.R., 2020. Phytoplankton dynamics in a changing Arctic Ocean. Nat. Climate Change 10 (10), 892–903. http://dx.doi.org/10.1038/s41558-020-0905-y.

Behrenfeld, M.J., 2014. Climate-mediated dance of the plankton. Nature Clim. Change 4 (10), 880–887. http://dx.doi.org/10.1038/nclimate2349.

Behrenfeld, M.J., Boss, E., Siegel, D.A., Shea, D.M., 2005. Carbon-based ocean productivity and phytoplankton physiology from space. Glob. Biogeochem. Cycles 19 (1), http://dx.doi.org/10.1029/2004GB002299.

Behrenfeld, M.J., O'Malley, R.T., Siegel, D.A., McClain, C.R., Sarmiento, J.L., Feldman, G.C., Milligan, A.J., Falkowski, P.G., Letelier, R.M., Boss, E.S., 2006. Climate-driven trends in contemporary ocean productivity. Nature 444 (7120), 752–755. http://dx.doi.org/10.1038/nature05317.

Bidigare, R.R., 2012. BiG RAPA water column HPLC pigments from R/V Melville MV1015 in the South Pacific from Arica, Chile to Easter Island. from November to 2010 (C-MORE project). Biological and Chemical Oceanography Data Management Office (BCO-DMO, Version Date 2012-11-05.

Bindoff, N.L., Cheung, W.W.L., Kairo, J.G., Arístegui, J., Guinder, V.A., Hallberg, R., Hilmi, N., Jiao, N., Karim, M.S., Levin, L., O'Donoghue, S., Cuicapusa, S.R.P., Rinkevich, B., Suga, T., Tagliabue, A., Williamson, P., 2019. Changing ocean, marine ecosystems, and dependent communities. In: Pörtner, H.-O., Roberts, D., Masson-Delmotte, V., Zhai, P., Tignor, M., Poloczanska, E., Mintenbeck, K., a, A.A., Nicolai, M., Okem, A., Petzold, J., Rama, B., Weyer, N. (Eds.), IPCC Special Report on the Ocean and Cryosphere in a Changing Climate. IPCC, pp. 448–587.

Bouman, H.A., Platt, T., Sathyendranath, S., Li, W.K.W., Stuart, V., Fuentes-Yaco, C., Maass, H., Horne, E.P.W., Ulloa, O., Lutz, V., Kyewalyanga, M., 2003. Temperature as indicator of optical properties and community structure of marine phytoplankton: implications for remote sensing. Mar. Ecol. Prog. Ser. 258, 19–30. http://dx.doi.org/10.3354/meps258019.

Boyce, D.G., Lewis, M.R., Worm, B., 2010. Global phytoplankton decline over the past century. Nature 466 (7306), 591–596. http://dx.doi.org/10.1038/nature09268.

Bracher, A., 2014a. Phytoplankton Pigment Concentrations During POLARSTERN Cruise ANT-XXVIII/3. Alfred Wegener Institute, Helmholtz Centre for Polar and Marine Research, Bremerhaven, http://dx.doi.org/10.1594/PANGAEA.848588.

Bracher, A., 2014b. Phytoplankton Pigments Measured on Water Bottle Samples During SONNE Cruise SO218. Alfred Wegener Institute, Helmholtz Centre for Polar and Marine Research, Bremerhaven, http://dx.doi.org/10.1594/PANGAEA.848589.

Bracher, A., 2015a. Phytoplankton Pigment Concentrations During Maria S. Merian Cruise MSM18/3. Alfred Wegener Institute, Helmholtz Centre for Polar and Marine Research, Bremerhaven, http://dx.doi.org/10.1594/PANGAEA.848586.

Bracher, A., 2015b. Phytoplankton Pigment Concentrations During POLARSTERN Cruise ANT-XXIV/1. Alfred Wegener Institute, Helmholtz Centre for Polar and Marine Research, Bremerhaven, http://dx.doi.org/10.1594/PANGAEA.848583.

Bracher, A., 2015c. Phytoplankton Pigment Concentrations During POLARSTERN Cruise ANT-XXIV/4. Alfred Wegener Institute, Helmholtz Centre for Polar and Marine Research, Bremerhaven, http://dx.doi.org/10.1594/PANGAEA.848584.

Bracher, A., 2015d. Phytoplankton Pigment Concentrations During POLARSTERN Cruise ANT-XXVI/4. Alfred Wegener Institute, Helmholtz Centre for Polar and Marine Research, Bremerhaven, http://dx.doi.org/10.1594/PANGAEA.848585.

Bracher, A., 2015e. Phytoplankton Pigment Concentrations During POLARSTERN Cruise ANT-XXVII/2. Alfred Wegener Institute, Helmholtz Centre for Polar and Marine Research, Bremerhaven, http://dx.doi.org/10.1594/PANGAEA.848590.

Bracher, A., 2019. Phytoplankton Pigment Concentrations in the Southern Ocean During RV POLARSTERN Cruise PS103 in Dec 2016 to Jan 2017. Alfred Wegener Institute, Helmholtz Centre for Polar and Marine Research, Bremerhaven, http://dx.doi.org/10.1594/PANGAEA.898941.

Bracher, A., Dinter, T., Wolanin, A., Rozanov, V.V., Losa, S.N., Soppa, M.A., 2017. Global monthly mean chlorophyll a surface concentrations from August 2002 to April 2012 for diatoms, coccolithophores and cyanobacteria from PhytoDOAS algorithm version 3.3 applied to SCIAMACHY data, link to NetCDF files in ZIP archive. http://dx.doi.org/10.1594/PANGAEA.870486.

Bracher, A., Taylor, B.B., 2017. Phytoplankton Pigment Concentrations Measured by HPLC During Maria S. Merian Cruise MSM9/1. Alfred Wegener Institute, Helmholtz Centre for Polar and Marine Research, Bremerhaven, http://dx.doi.org/10.1594/PANGAEA.873070.

Bracher, A., Taylor, M.H., Taylor, B.B., Dinter, T., Röttgers, R., Steinmetz, F., 2015. Phytoplankton pigment concentrations during POLARSTERN cruise ANT-XXIII/1. http://dx.doi.org/10.1594/PANGAEA.871713.

Bracher, A., Tilzer, M., 2001. Underwater light field and phytoplankton absorbance in different surface water masses of the Atlantic sector of the Southern Ocean. Polar Biol. 24 (9), 687–696. http://dx.doi.org/10.1007/s003000100269.

Bracher, A., Vountas, M., Dinter, T., Burrows, J.P., Röttgers, R., Peeken, I., 2009. Quantitative observation of cyanobacteria and diatoms from space using PhytoDOAS on SCIAMACHY data. Biogeosciences 6 (5), 751–764. http://dx.doi.org/10.5194/bg-6-751-2009.

Bracher, A., Wiegmann, S., 2019. Phytoplankton Pigment Concentrations in the North Sea and Sogne Fjord from 29 April to 7 2016 During RV HEINCKE Cruise HE462. Alfred Wegener Institute, Helmholtz Centre for Polar and Marine Research, Bremerhaven, http://dx.doi.org/10.1594/PANGAEA.899043.

Bracher, A., Wiegmann, S., Xi, H., Dinter, T., 2020. Phytoplankton pigment concentration and phytoplankton groups measured on water samples obtained during POLARSTERN cruise PS113 in the Atlantic Ocean. http://dx.doi.org/10.1594/PANGAEA.911061.

Brewin, R.J.W., Ciavatta, S., Sathyendranath, S., Jackson, T., Tilstone, G., Curran, K., Airs, R.L., Cummings, D., Brotas, V., Organelli, E., Dall'Olmo, G., Raitsos, D.E., 2017. Uncertainty in ocean-color estimates of chlorophyll for phytoplankton groups. Front. Mar. Sci. 4, http://dx.doi.org/10.3389/fmars.2017.00104.

Brewin, R.J.W., Ciavatta, S., Sathyendranath, S., Skákala, J., Bruggeman, J., Ford, D., Platt, T., 2019a. The influence of temperature and community structure on light absorption by phytoplankton in the north atlantic. Sensors 19 (19), 4182. http://dx.doi.org/10.3390/s19194182.

Brewin, R.J.W., Dall'Olmo, G., Gittings, J., Sun, X., Lange, P.K., Raitsos, D.E., Bouman, H.A., Hoteit, I., Aiken, J., Sathyendranath, S., 2022. A conceptual approach to partitioning a vertical profile of phytoplankton biomass into contributions from two communities. J. Geophys. Res.: Oceans 127 (4), http://dx.doi.org/10.1029/2021JC018195.

Brewin, R.J.W., Devred, E., Sathyendranath, S., Lavender, S.J., Hardman-Mountford, N.J., 2011. Model of phytoplankton absorption based on three size classes. Appl. Opt. 50 (22), 4535. http://dx.doi.org/10.1364/ao.50.004535.

Brewin, R.J.W., Mélin, F., Sathyendranath, S., Steinmetz, F., Chuprin, A., Grant, M., 2014a. On the temporal consistency of chlorophyll products derived from three ocean-colour sensors. ISPRS J. Photogram. Remote Sens. 97, 171–184. http://dx.doi.org/10.1016/j.isprsjprs.2014.08.013.

Brewin, R.J.W., Morán, X.A.G., Raitsos, D.E., Gittings, J.A., Calleja, M.L., Viegas, M., Ansari, M.I., Al-Otaibi, N., Huete-Stauffer, T.M., Hoteit, I., 2019b. Factors regulating the relationship between total and size-fractionated chlorophyll-a in coastal waters of the red sea. Front. Microbiol. 10, http://dx.doi.org/10.3389/fmicb.2019.01964.

Brewin, R.J.W., Sathyendranath, S., Bricaud, A., Ciotti, A., Devred, E., Hirata, T., Kostadinov, T.S., Loisel, H., Mouw, C.B., Uitz, J., 2014b. Detection of phytoplankton size structure by remote sensing. In: Sathyendranath, S. (Ed.), Phytoplankton Functional Types from Space. Reports of the International Ocean-Colour Coordinating Group, No. 15, IOCCG, Dartmouth, Canada, pp. 71–100.

Brewin, R.J.W., Sathyendranath, S., Hirata, T., Lavender, S.J., Barciela, R.M., Hardman-Mountford, N.J., 2010. A three-component model of phytoplankton size class for the Atlantic Ocean. Ecol. Model. 221 (11), 1472–1483. http://dx.doi.org/10.1016/j.ecolmodel.2010.02.014.

Brewin, R.J.W., Sathyendranath, S., Jackson, T., Barlow, R., Brotas, V., Airs, R., Lamont, T., 2015. Influence of light in the mixed-layer on the parameters of a three-component model of phytoplankton size class. Remote Sens. Environ. 168, 437–450. http://dx.doi.org/10.1016/j.rse.2015.07.004.

Brewin, R.J.W., Sathyendranath, S., Lange, P.K., Tilstone, G., 2014c. Comparison of two methods to derive the size-structure of natural populations of phytoplankton. Deep Sea Res. Part I 85, 72–79. http://dx.doi.org/10.1016/j.dsr.2013.11.007.

Brewin, R.J.W., Sathyendranath, S., Platt, T., Bouman, H., Ciavatta, S., Dall'Olmo, G., Dingle, J., Groom, S., Jönsson, B., Kostadinov, T.S., Kulk, G., Laine, M., Martínez-Vicente, V., Psarra, S., Raitsos, D.E., Richardson, K., Rio, M.-H., Rousseaux, C.S., Salisbury, J., Shutler, J.D., Walker, P., 2021. Sensing the ocean biological carbon pump from space: A review of capabilities, concepts, research gaps and future developments. Earth-Sci. Rev. 217, 103604. http://dx.doi.org/10.1016/j.earscirev.2021.103604.

Brewin, R.J.W., Sathyendranath, S., Tilstone, G., Lange, P.K., Platt, T., 2014d. A multicomponent model of phytoplankton size structure. J. Geophys. Res.: Oceans 119 (6), 3478–3496. http://dx.doi.org/10.1002/2014JC009859.

Bulgin, C.E., Merchant, C.J., Ferreira, D., 2020. Tendencies, variability and persistence of sea surface temperature anomalies. Sci. Rep. 10 (1), http://dx.doi.org/10.1038/s41598-020-64785-9.

California Current Ecosystem LTER, Goericke, R., 2018. Size fractionation for total chl a within the surface layer and calculated size distribution of total chl a from discrete bottle samples from CCE-calcofi augmented cruises in the california current system, 2004 - 2017 (ongoing). http://dx.doi.org/10.6073/pasta/8ebed2a2ac22a27b23e7ba98f10dcbb4.

Cermeño, P., Dutkiewicz, S., Harris, R.P., Follows, M., Schofield, O., Falkowski, P.G., 2008. The role of nutricline depth in regulating the ocean carbon cycle. Proc. Natl. Acad. Sci. 105 (51), 20344–20349. http://dx.doi.org/10.1073/pnas.0811302106.

Chase, A., Boss, E., Zaneveld, R., Bricaud, A., Claustre, H., Ras, J., Dall'Olmo, G., Westberry, T.K., 2013. Decomposition of in situ particulate absorption spectra. Methods Oceanogr. 7, 110–124. http://dx.doi.org/10.1016/j.mio.2014.02.002.

Claustre, H., 2013. Pigment concentrations in surface water during THALASSA campaign PROSOPE. http://dx.doi.org/10.1594/PANGAEA.805388.

Claustre, H., Hooker, S.B., Heukelem, L.V., Berthon, J.-F., Barlow, R., Ras, J., Sessions, H., Targa, C., Thomas, C.S., van der Linde, D., Marty, J.-C., 2004. An intercomparison of HPLC phytoplankton pigment methods using in situ samples: application to remote sensing and database activities. Mar. Chem. 85 (1–2), 41–61. http://dx.doi.org/10.1016/j.marchem.2003.09.002.

Clayton, S., Nagai, T., Follows, M.J., 2014. (Supplement 1) Hydrochemistry and phytoplankton pigments in water samples obtained during R/V Natsushima (JAMSTEC) cruise to the Kuroshio Extension Front in October 2009. http://dx.doi.org/10.1594/PANGAEA.819108.

Cota, G.F., Hill, V.J., 2007a. HLY-02-01 High Performance Liquid Chromatography (HPLC) Pigment [Hill, V.]. http://dx.doi.org/10.5065/D6FF3QGJ.

Cota, G.F., Hill, V.J., 2007b. HLY-02-03 High Performance Liquid Chromatography (HPLC) Pigment Data [Hill, V.]. http://dx.doi.org/10.5065/D66M34XW.

de Boyer Montégut, C., Madec, G., Fischer, A.S., Lazar, A., Iudicone, D., 2004. Mixed layer depth over the global ocean: An examination of profile data and a profile-based climatology. J. Geophys. Res. 109 (C12), http://dx.doi.org/10.1029/2004JC002378.

Defoin-Platel, M., Chami, M., 2007. How ambiguous is the inverse problem of ocean color in coastal waters? J. Geophys. Res. 112 (C3), http://dx.doi.org/10.1029/2006JC003847.

Devred, E., Sathyendranath, S., Stuart, V., Maass, H., Ulloa, O., Platt, T., 2006. A two-component model of phytoplankton absorption in the open ocean: Theory and applications. J. Geophys. Res. 111 (C3), http://dx.doi.org/10.1029/2005JC002880.

Devred, E., Sathyendranath, S., Stuart, V., Platt, T., 2011. A three component classification of phytoplankton absorption spectra: Application to ocean-color data. Remote Sens. Environ. 115 (9), 2255–2266. http://dx.doi.org/10.1016/j.rse.2011.04.025.

Dierssen, H.M., 2010. Perspectives on empirical approaches for ocean color remote sensing of chlorophyll in a changing climate. Proc. Natl. Acad. Sci. 107 (40), 17073–17078. http://dx.doi.org/10.1073/pnas.0913800107.

Dierssen, H.M., Ackleson, S.G., Joyce, K.E., Hestir, E.L., Castagna, A., Lavender, S., McManus, M.A., 2021. Living up to the hype of hyperspectral aquatic remote sensing: Science, resources and outlook. Front. Environ. Sci. 9, http://dx.doi.org/10.3389/fenvs.2021.649528.

Dierssen, H.M., Smith, R.C., 2000. Bio-optical properties and remote sensing ocean color algorithms for Antarctic Peninsula waters. J. Geophys. Res.: Oceans 105 (C11), 26301–26312. http://dx.doi.org/10.1029/1999JC000296.

Dierssen, H.M., Vernet, M., Smith, R.C., 2000. Optimizing models for remotely estimating primary production in Antarctic coastal waters. Antarct. Sci. 12 (1), 20–32. http://dx.doi.org/10.1017/S0954102000000043.

DiTullio, G., 2011. HPLC Analyses of Algal Pigment Concentrations from the Cofemug Cruise (KN192-05) in the South Atlantic Subtropical Gyre During 2007. Biological and Chemical Oceanography Data Management Office (BCO-DMO), Version Date 2011-05-18.

DiTullio, G., 2015. Sample HPLC Pigments from RVIB Nathaniel B. Palmer NBP1302 Cruise in the Ross Sea During 2013 (TRACERS Project). Biological and Chemical Oceanography Data Management Office (BCO-DMO), Version Date 2015-05-18.

DiTullio, G., Lee, P., 2019a. Algal Pigment Concentrations Measured by HPLC from RVIB Nathaniel B. Palmer Cruise in the Ross Sea, Southern Ocean from 2017-2018. Biological and Chemical Oceanography Data Management Office (BCO-DMO), http://dx.doi.org/10.1575/1912/bco-dmo.778881.2, (Version 2) Version Date 2019-12-24.

DiTullio, G., Lee, P., 2019b. Algal pigment concentrations, High Arctic, August-September 2018. Arctic Data Center. http://dx.doi.org/10.18739/A2028PD2H.

Dow, K., Downing, T.E., 2016. the Atlas of Climate Change. University of California Press, http://dx.doi.org/10.1525/9780520966826.

European Union-Copernicus Marine Service, 2019. Global Ocean Sea Surface Temperature trend map from Observations Reprocessing. http://dx.doi.org/10.48670/moi-00243.

Falkowski, P.G., Barber, R.T., Smetacek, V., 1998. Biogeochemical controls and feedbacks on ocean primary production. Science 281 (5374), 200–206. http://dx.doi.org/10.1126/science.281.5374.200.

Ferreira, A., Costa, R.R., Dotto, T.S., Kerr, R., Tavano, V.M., Brito, A.C., Brotas, V., Secchi, E.R., Mendes, C.R.B., 2020. Changes in phytoplankton communities along the northern antarctic peninsula: Causes, impacts and research priorities. Front. Mar. Sci. 7, http://dx.doi.org/10.3389/fmars.2020.576254.

Field, C.B., Behrenfeld, M.J., Randerson, J.T., Falkowski, P., 1998. Primary production of the biosphere: Integrating terrestrial and oceanic components. Science 281 (5374), 237–240. http://dx.doi.org/10.1126/science.281.5374.237.

Finkel, Z.V., Beardall, J., Flynn, K.J., Quigg, A., Rees, T.A.V., Raven, J.A., 2009. Phytoplankton in a changing world: cell size and elemental stoichiometry. J. Plankton Res. 32 (1), 119–137. http://dx.doi.org/10.1093/plankt/fbp098.

Flombaum, P., Gallegos, J.L., Gordillo, R.A., Rincón, J., Zabala, L.L., Jiao, N., Karl, D.M., Li, W.K.W., Lomas, M.W., Veneziano, D., Vera, C.S., Vrugt, J.A., Martiny, A.C., 2013. Present and future global distributions of the marine Cyanobacteria *Prochlorococcus* and *Synechococcus*. Proc. Natl. Acad. Sci. 110 (24), 9824–9829. http://dx.doi.org/10.1073/pnas.1307701110.

Flombaum, P., Martiny, A.C., 2021. Diverse but uncertain responses of picophytoplankton lineages to future climate change. Limnol. Oceanogr. 66 (12), 4171–4181. http://dx.doi.org/10.1002/lno.11951.

Flombaum, P., Wang, W.-L., Primeau, F.W., Martiny, A.C., 2020. Global picophytoplankton niche partitioning predicts overall positive response to ocean warming. Nat. Geosci. 13 (2), 116–120. http://dx.doi.org/10.1038/s41561-019-0524-2.

Friedlingstein, P., Jones, M.W., O'Sullivan, M., Andrew, R.M., Bakker, D.C.E., Hauck, J., Quéré, C.L., Peters, G.P., Peters, W., Pongratz, J., Sitch, S., Canadell, J.G., Ciais, P., Jackson, R.B., Alin, S.R., Anthoni, P., Bates, N.R., Becker, M., Bellouin, N., Bopp, L., Chau, T.T.T., Chevallier, F., Chini, L.P., Cronin, M., Currie, K.I., Decharme, B., Djeutchouang, L., Dou, X., Evans, W., Feely, R.A., Feng, L., Gasser, T., Gilfillan, D., Gkritzalis, T., Grassi, G., Gregor, L., Gruber, N., Gürses, Ö., Harris, I., Houghton, R.A., Hurtt, G.C., Iida, Y., Ilyina, T., Luijkx, I.T., Jain, A.K., Jones, S.D., Kato, E., Kennedy, D., Goldewijk, K.K., Knauer, J., Korsbakken, J.I., Körtzinger, A., Landschützer, P., Lauvset, S.K., Lefèvre, N., Lienert, S., Liu, J., Marland, G., McGuire, P.C., Melton, J.R., Munro, D.R., Nabel, J.E.M.S., Nakaoka, S.-I., Niwa, Y., Ono, T., Pierrot, D., Poulter, B., Rehder, G., Resplandy, L., Robertson, E., Rödenbeck, C., Rosan, T.M., Schwinger, J., Schwingshackl, C., Séférian, R., Sutton, A.J., Sweeney, C., Tanhua, T., Tans, P.P., Tian, H., Tilbrook, B., Tubiello, F., van der Werf, G., Vuichard, N., Wada, C., Wanninkhof, R., Watson, A., Willis, D., Wiltshire, A.J., Yuan, W., Yue, C., Yue, X., Zaehle, S., Zeng, J., 2021. Global carbon budget 2021. Earth Syst. Sci. Data http://dx.doi.org/10.5194/essd-2021-386, [preprint].

Garver, S.A., Siegel, D.A., 1997. Inherent optical property inversion of ocean color spectra and its biogeochemical interpretation: 1. Time series from the Sargasso Sea. J. Geophys. Res.: Oceans 102 (C8), 18607–18625. http://dx.doi.org/10.1029/96JC03243.

GCOS, 2011. Systematic observation requirements for satellite-based products for climate supplemental details to the satellite-based component of the implementation plan for the global observing system for climate in support of the UNFCCC: 2011 update. Tech. rep., World Meteorological Organization (WMO) ; United Nations Educational, Scientific and Cultural Organization ; United Nations Environment Programme ; International Council for Science.

Gholizadeh, H., Robeson, S.M., 2016. Revisiting empirical ocean-colour algorithms for remote estimation of chlorophyll-a content on a global scale. Int. J. Remote Sens. 37 (11), 2682–2705. http://dx.doi.org/10.1080/01431161.2016.1183834.

Gin, K.Y.-H., Lin, X., Zhang, S., 2000. Dynamics and size structure of phytoplankton in the coastal waters of Singapore. J. Plankton Res. 22 (8), 1465–1484. http://dx.doi.org/10.1093/plankt/22.8.1465.

Gittings, J.A., Raitsos, D.E., Krokos, G., Hoteit, I., 2018. Impacts of warming on phytoplankton abundance and phenology in a typical tropical marine ecosystem. Sci. Rep. 8 (1), http://dx.doi.org/10.1038/s41598-018-20560-5.

Goericke, R., 2002. Top-down control of phytoplankton biomass and community structure in the monsoonal Arabian Sea. Limnol. Oceanogr. 47 (5), 1307–1323. http://dx.doi.org/10.4319/lo.2002.47.5.1307.

Gregg, W.W., Rousseaux, C.S., 2019. Global ocean primary production trends in the modern ocean color satellite record (1998–2015). Environ. Res. Lett. 14 (12), 124011. http://dx.doi.org/10.1088/1748-9326/ab4667.

Hammond, M.L., Beaulieu, C., Henson, S.A., Sahu, S.K., 2020. Regional surface chlorophyll trends and uncertainties in the global ocean. Sci. Rep. 10 (1), http://dx.doi.org/10.1038/s41598-020-72073-9.

Hays, G.C., Richardson, A.J., Robinsone, C., 2005. Climate change and marine plankton. Trends Ecol. Evol. 20 (6), 337–344. http://dx.doi.org/10.1016/j.tree.2005.03.004.

Henson, S.A., Sarmiento, J.L., Dunne, J.P., Bopp, L., Lima, I., Doney, S.C., John, J., Beaulieu, C., 2010. Detection of anthropogenic climate change in satellite records of ocean chlorophyll and productivity. Biogeosciences 7 (2), 621–640. http://dx.doi.org/10.5194/bg-7-621-2010.

Hepach, H., Quack, B., Tegtmeier, S., Engel, A., Bracher, A., Fuhlbrügge, S., Galgani, L., Atlas, E.L., Lampel, J., Frieß, U., Krüger, K., 2016. Pigment measured on water bottle samples during METEOR cruise M91. http://dx.doi.org/10.1594/PANGAEA.864786.

Hill, V.J., 2007a. HLY-04-02 High Performance Liquid Chromatography (HPLC) Pigment Data. [Hill, V.]. http://dx.doi.org/10.5065/D6GH9G13.

Hill, V.J., 2007b. HLY-04-03 High Performance Liquid Chromatography (HPLC) Pigment Data. [Hill, V.]. http://dx.doi.org/10.5065/D6RR1WBZ.

Hirata, T., Hardman-Mountford, N.J., Brewin, R.J.W., Aiken, J., Barlow, R., Suzuki, K., Isada, T., Howell, E., Hashioka, T., Noguchi-Aita, M., Yamanaka, Y., 2011. Synoptic relationships between surface Chlorophyll-a and diagnostic pigments specific to phytoplankton functional types. Biogeosciences 8 (2), 311–327. http://dx.doi.org/10.5194/bg-8-311-2011.

Hoegh-Guldberg, O., Bruno, J.F., 2010. The impact of climate change on the world's marine ecosystems. Science 328 (5985), 1523–1528. http://dx.doi.org/10.1126/science.1189930.

IMOS, 2021a. IMOS - SRS - ocean colour - bio optical database of Australian waters.

IMOS, 2021b. IMOS national reference station (NRS) - phytoplankton HPLC pigment composition analysis.

Jackson, T., Sathyendranath, S., Platt, T., 2017. An exact solution for modeling photoacclimation of the carbon-to-chlorophyll ratio in phytoplankton. Front. Mar. Sci. 4, http://dx.doi.org/10.3389/fmars.2017.00283.

Johnson, G.C., Lyman, J.M., 2020. Warming trends increasingly dominate global ocean. Nature Clim. Change 10 (8), 757–761. http://dx.doi.org/10.1038/s41558-020-0822-0.

Kahru, M., Brotas, V., Manzano-Sarabia, M., Mitchell, B.G., 2010. Are phytoplankton blooms occurring earlier in the Arctic? Global Change Biol. 17 (4), 1733–1739. http://dx.doi.org/10.1111/j.1365-2486.2010.02312.x.

Korb, R.E., Whitehouse, M.J., Ward, P., 2004. SeaWiFS in the southern ocean: spatial and temporal variability in phytoplankton biomass around South Georgia. Deep Sea Res. Part II 51 (1–3), 99–116. http://dx.doi.org/10.1016/j.dsr2.2003.04.002.

Kulk, G., Platt, T., Dingle, J., Jackson, T., Jönsson, B., Bouman, H., Babin, M., Brewin, R., Doblin, M., Estrada, M., Figueiras, F., Furuya, K., González-Benítez, N., Gudfinnsson, H., Gudmundsson, K., Huang, B., Isada, T., Kovač, Ž., Lutz, V., Marañón, E., Raman, M., Richardson, K., Rozema, P., Poll, W., Segura, V., Tilstone, G., Uitz, J., Dongen-Vogels, V., Yoshikawa, T., Sathyendranath, S., 2020. Primary production, an index of climate change in the ocean: Satellite-based estimates over two decades. Remote Sens. 12 (5), 826. http://dx.doi.org/10.3390/rs12050826.

Landry, M.R., 2021. Phytoplankton HPLC Pigment Concentrations from Samples Collected in the Gulf of Mexico on R/V Nancy Foster Cruises in 2017 and 2018. Biological and Chemical Oceanography Data Management Office (BCO-DMO), http://dx.doi.org/10.26008/1912/bco-dmo.851250.1, (Version 1) Version Date 2021-05-03.

Lange, P., Brewin, R., Dall'Olmo, G., Tarran, G., Sathyendranath, S., Zubkov, M., Bouman, H., 2018. Scratching beneath the surface: A model to predict the vertical distribution of *Prochlorococcus* using remote sensing. Remote Sens. 10 (6), 847. http://dx.doi.org/10.3390/rs10060847.

Lee, P., 2020. HPLC Pigment Data from Samples Collected During R/V Savannah Cruises Conducted in the South Atlantic Bight Off the Coast of Georgia from 2015-2017. Biological and Chemical Oceanography Data Management Office (BCO-DMO, http://dx.doi.org/10.26008/1912/bco-dmo.816216.1, (Version 1) Version Date 2020-06-19.

Li, W.K.W., McLaughlin, F.A., Lovejoy, C., Carmack, E.C., 2009. Smallest algae thrive as the arctic ocean freshens. Science 326 (5952), 539. http://dx.doi.org/10.1126/science.1179798.

Liu, Y., Hellmann, S., Wiegmann, S., Bracher, A., 2019. Phytoplankton pigment concentrations measured by HPLC during POLARSTERN cruise PS99.1. http://dx.doi.org/10.1594/PANGAEA.905502.

Liu, H., Liu, X., Xiao, W., Laws, E.A., Huang, B., 2021. Spatial and temporal variations of satellite-derived phytoplankton size classes using a three-component model bridged with temperature in Marginal Seas of the Western Pacific Ocean. Prog. Oceanogr. 191, 102511. http://dx.doi.org/10.1016/j.pocean.2021.102511.

Lombard, F., Boss, E., Waite, A.M., Vogt, M., Uitz, J., Stemmann, L., Sosik, H.M., Schulz, J., Romagnan, J.-B., Picheral, M., Pearlman, J., Ohman, M.D., Niehoff, B., Möller, K.O., Miloslavich, P., Lara-Lpez, A., Kudela, R., Lopes, R.M., Kiko, R., Karp-Boss, L., Jaffe, J.S., Iversen, M.H., Irisson, J.-O., Fennel, K., Hauss, H., Guidi, L., Gorsky, G., Giering, S.L.C., Gaube, P., Gallager, S., Dubelaar, G., Cowen, R.K., Carlotti, F., Briseño-Avena, C., Berline, L., Benoit-Bird, K., Bax, N., Batten, S., Ayata, S.D., Artigas, L.F., Appeltans, W., 2019. Globally consistent quantitative observations of planktonic ecosystems. Front. Mar. Sci. 6, http://dx.doi.org/10.3389/fmars.2019.00196.

Longhurst, A., Sathyendranath, S., Platt, T., Caverhill, C., 1995. An estimate of global primary production in the ocean from satellite radiometer data. J. Plankton Res. 17 (6), 1245–1271. http://dx.doi.org/10.1093/plankt/17.6.1245.

López-Urrutia, Á., Morán, X.A.G., 2015. Temperature affects the size-structure of phytoplankton communities in the ocean. Limnol. Oceanogr. 60 (3), 733–738. http://dx.doi.org/10.1002/lno.10049.

Losa, S.N., Soppa, M.A., Dinter, T., Wolanin, A., Brewin, R.J.W., Bricaud, A., Oelker, J., Peeken, I., Gentili, B., Rozanov, V., Bracher, A., 2017. Synergistic exploitation of hyper- and multi-spectral precursor sentinel measurements to determine phytoplankton functional types (SynSenPFT). Front. Mar. Sci. 4, http://dx.doi.org/10.3389/fmars.2017.00203.

Lubac, B., Loisel, H., Guiselin, N., Astoreca, R., Artigas, L.F., Mériaux, X., 2008. Hyperspectral and multispectral ocean color inversions to detect *Phaeocystis globosa* blooms in coastal waters. J. Geophys. Res. 113 (C6), http://dx.doi.org/10.1029/2007JC004451.

Marañón, E., Cermeño, P., Latasa, M., Tadonléké, R.D., 2012. Temperature, resources, and phytoplankton size structure in the ocean. Limnol. Oceanogr. 57 (5), 1266–1278. http://dx.doi.org/10.4319/lo.2012.57.5.1266.

Marañón, E., Cermeño, P., Latasa, M., Tadonléké, R.D., 2015. Resource supply alone explains the variability of marine phytoplankton size structure. Limnol. Oceanogr. 60 (5), 1848–1854. http://dx.doi.org/10.1002/lno.10138.

Marinov, I., Doney, S.C., Lima, I.D., 2010. Response of ocean phytoplankton community structure to climate change over the 21st century: partitioning the effects of nutrients, temperature and light. Biogeosciences 7 (12), 3941–3959. http://dx.doi.org/10.5194/bg-7-3941-2010.

Maritorena, S., Siegel, D.A., Peterson, A.R., 2002. Optimization of a semianalytical ocean color model for global-scale applications. Appl. Opt. 41 (15), 2705. http://dx.doi.org/10.1364/AO.41.002705.

Martinez, E., Antoine, D., D'Ortenzio, F., Gentili, B., 2009. Climate-driven basin-scale decadal oscillations of oceanic phytoplankton. Science 326 (5957), 1253–1256. http://dx.doi.org/10.1126/science.1177012.

McClain, C.R., 2009. A decade of satellite ocean color observations. Ann. Rev. Mar. Sci. 1 (1), 19–42. http://dx.doi.org/10.1146/annurev.marine.010908.163650.

McGillicuddy, D., 2007a. HPLC pigments, EDDIES WB cruises from R/V Weatherbird II WB0409, WB0413, WB0506, WB0508 in the Sargasso Sea from 2004-2005 (EDDIES project). Biological and Chemical Oceanography Data Management Office (BCO-DMO), http://dx.doi.org/10.1575/1912/bco-dmo.3023.1, (Version 1) Version Date 2007-03-13.

McGillicuddy, D., 2007b. Pigments from HPLC analysis of bottle samples collected during R/V Oceanus cruises OC404-01, OC404-04, OC415-01 and OC415-03 from the Sargasso Sea, June 11, 2004 to August 24, 2005 (EDDIES project). Biological and Chemical Oceanography Data Management Office (BCO-DMO), http://dx.doi.org/10.1575/1912/5075, Version Date 2007-11-01.

Merchant, C.J., Embury, O., Bulgin, C.E., Block, T., Corlett, G.K., Fiedler, E., Good, S.A., Mittaz, J., Rayner, N.A., Berry, D., Eastwood, S., Taylor, M., Tsushima, Y., Waterfall, A., Wilson, R., Donlon, C., 2019. Satellite-based time-series of sea-surface temperature since 1981 for climate applications. Sci. Data 6 (1), http://dx.doi.org/10.1038/s41597-019-0236-x.

Minnett, P.J., Alvera-Azcárate, A., Chin, T.M., Corlett, G.K., Gentemann, C.L., Karagali, I., Li, X., Marsouin, A., Marullo, S., Maturi, E., Santoleri, R., Picart, S.S., Steele, M., Vazquez-Cuervo, J., 2019. Half a century of satellite remote sensing of sea-surface temperature. Remote Sens. Environ. 233, 111366. http://dx.doi.org/10.1016/j.rse.2019.111366.

Mitchell, B.G., Holm-Hansen, O., 1991. Bio-optical properties of Antarctic Peninsula waters: differentiation from temperate ocean models. Deep Sea Res. Part A 38 (8–9), 1009–1028. http://dx.doi.org/10.1016/0198-0149(91)90094-V.

Montes-Hugo, M., Doney, S.C., Ducklow, H.W., Fraser, W., Martinson, D., Stammerjohn, S.E., Schofield, O., 2009. Recent changes in phytoplankton communities associated with rapid regional climate change along the western antarctic peninsula. Science 323 (5920), 1470–1473. http://dx.doi.org/10.1126/science.1164533.

Moore, T.S., Brown, C.W., 2020. Incorporating environmental data in abundance-based algorithms for deriving phytoplankton size classes in the Atlantic Ocean. Remote Sens. Environ. 240, 111689. http://dx.doi.org/10.1016/j.rse.2020.111689.

Morán, S.A.G., López-Urrutia, A., Calvo-Díaz, A., Li, W.K.W., 2010. Increasing importance of small phytoplankton in a warmer ocean. Global Change Biol. 16 (3), 1137–1144. http://dx.doi.org/10.1111/j.1365-2486.2009.01960.x.

Mouw, C.B., Ciochetto, A.B., Yoder, J.A., 2019. A satellite assessment of environmental controls of phytoplankton community size structure. Glob. Biogeochem. Cycles 33, 540–558. http://dx.doi.org/10.1029/2018GB006118.

O'Reilly, J.E., Maritorena, S., Mitchell, B.G., Siegel, D.A., Carder, K.L., Garver, S.A., Kahru, M., McClain, C., 1998. Ocean color chlorophyll algorithms for SeaWiFS. J. Geophys. Res.: Oceans 103 (C11), 24937–24953. http://dx.doi.org/10.1029/98JC02160.

Palmer Station Antarctica LERT, Schofield, O., Vernet, M., Prezelin, B., 2018. Photosynthetic pigments of water column samples and analyzed with High Performance Liquid Chromatography (HPLC), collected aboard Palmer LTER annual cruises off the coast of the Western Antarctica Peninsula, 1991 - 2016. http://dx.doi.org/10.6073/pasta/4d583713667a0f52b9d2937a26d0d82e.

Palmer Station Antarctica LTER, Schofield, O., Vernet, M., Prezelin, B., 2020. Photosynthetic pigments of water column samples analyzed using High Performance Liquid Chromatography (HPLC), sampled during the Palmer LTER field seasons at Palmer Station, Antarctica, 1991 – 2015. http://dx.doi.org/10.6073/PASTA/EC55E3D0D7260E1DF98C9156F9BECDEB.

Peeken, I., Bluhm, K., Zöllner, E., 2017a. Phytoplankton pigments measured from underway and water bottle samples during Marion Dufresne cruise MD158 (OOMPH MD07 leg 1). http://dx.doi.org/10.1594/PANGAEA.873203.

Peeken, I., Bluhm, K., Zöllner, E., 2017b. Phytoplankton pigments measured from underway and water bottle samples during Marion Dufresne cruise MD160 (OOMPH MD07 leg 2). http://dx.doi.org/10.1594/PANGAEA.873208.

Peeken, I., Bracher, A., Murawski, S., 2017c. Phytoplankton pigments measured on water bottle samples during POLARSTERN cruise ANT-XXIV/2. http://dx.doi.org/10.1594/PANGAEA.873199.

Peeken, I., Hoffmann, L., 2014. Phytoplankton pigments and nutrients measured on water bottle samples during METEOR cruise M55. http://dx.doi.org/10.1594/PANGAEA.869828.

Peeken, I., Nachtigall, K., 2014a. Phytoplankton pigments measured on water bottle samples during POLARSTERN cruise ANT-XVIII/2 (EisenEx). http://dx.doi.org/10.1594/PANGAEA.869823.

Peeken, I., Nachtigall, K., 2014b. Phytoplankton pigments measured on water bottle samples during POLARSTERN cruise ANT-XXVI/3. http://dx.doi.org/10.1594/PANGAEA.869826.

Peeken, I., Nachtigall, K., 2014c. Pigments measured on water bottle samples during METEOR cruise M60. http://dx.doi.org/10.1594/PANGAEA.869830.

Peeken, I., Quack, B., 2017. Phytoplankton pigments measured on underway and water bottle samples during POSEIDON cruise POS320. http://dx.doi.org/10.1594/PANGAEA.873198.

Peeken, I., Walter, S., 2017. Phytoplankton pigments measured from underway and water bottle samples during POSEIDON cruise POS348. http://dx.doi.org/10.1594/PANGAEA.873200.

Peeken, I., Wilken, S., Bremer, K., Schnack-Schiel, S.B., 2017d. Phytoplankton pigments measured from seawater samples from the Spermonde Archipelago in southwest Sulawesi, Indonesia. http://dx.doi.org/10.1594/PANGAEA.873209.

Platt, T., Sathyendranath, S., 2008. Ecological indicators for the pelagic zone of the ocean from remote sensing. Remote Sens. Environ. 112 (8), 3426–3436. http://dx.doi.org/10.1016/j.rse.2007.10.016.

Racault, M.-F., Quéré, C.L., Buitenhuis, E., Sathyendranath, S., Platt, T., 2012. Phytoplankton phenology in the global ocean. Ecol. Indic. 14 (1), 152–163. http://dx.doi.org/10.1016/j.ecolind.2011.07.010.

Raimbault, P., Taupier-Letage, I., Rodier, M., 1988. Vertical size distribution of phytoplankton in the western Mediterranean Sea during early summer. Mar. Ecol. Prog. Ser. 45 (1/2), 153–158.

Reynolds, R.A., Stramski, D., Mitchell, B.G., 2001. A chlorophyll-dependent semianalytical reflectance model derived from field measurements of absorption and backscattering coefficients within the Southern Ocean. J. Geophys. Res.: Oceans 106 (C4), 7125–7138. http://dx.doi.org/10.1029/1999JC000311.

Rhein, M., Rintoul, S.R., Aoki, S., Campos, E., Chambers, D., Feely, R.A., Gulev, S., Johnson, G.C., Josey, S.A., AndreyKostianoy, Mauritzen, C., Roemmich, D., Talley, L.D., Wang, F., 2013. Observations: Ocean. In: Stocker, T.F., Qin, D., Plattner, G.-K., Tignor, M., Allen, S.K., Boschung, J., Nauels, A., Xia, Y., Bex, V., Midgley, P.M. (Eds.), Climate Change 2013: The Physical Science Basis. Contribution of Working Group I to the Fifth Assessment Report of the Intergovernmental Panel on Climate Change. Cambridge University Press, Cambridge, United Kingdom and New York, NY, USA, pp. 255–315.

Richardson, T., Condon, R., Neuer, S., 2013. Pigment concentrations (HPLC) from R/V Atlantic Explorer cruises AE1102, AE1118, AE1206, AE1219 in the Sargasso Sea, Bermuda Atlantic Time-Series Station (BATS) from 2011-2012 (Trophic BATS project). Biological and Chemical Oceanography Data Management Office (BCO-DMO), http://dx.doi.org/10.1575/1912/bco-dmo.3884.1, (Version 1) Version Date 2013-06-14.

Robinson, A., Bouman, H.A., Tilstone, G.H., Sathyendranath, S., 2018. Size class dependent relationships between temperature and phytoplankton photosynthesis-irradiance parameters in the atlantic ocean. Front. Mar. Sci. http://dx.doi.org/10.3389/fmars.2017.00435.

Robinson, C.M., Huot, Y., Schuback, N., Ryan-Keogh, T.J., Thomalla, S.J., Antoine, D., 2021. High latitude Southern Ocean phytoplankton have distinctive bio-optical properties. Opt. Express 29 (14), 21084. http://dx.doi.org/10.1364/OE.426737.

Sathyendranath, S., Brewin, R., Brockmann, C., Brotas, V., Calton, B., Chuprin, A., Cipollini, P., Couto, A., Dingle, J., Doerffer, R., Donlon, C., Dowell, M., Farman, A., Grant, M., Groom, S., Horseman, A., Jackson, T., Krasemann, H., Lavender, S., Martinez-Vicente, V., Mazeran, C., Mélin, F., Moore, T., Müller, D., Regner, P., Roy, S., Steele, C., Steinmetz, F., Swinton, J., Taberner, M., Thompson, A., Valente, A., Zühlke, M., Brando, V., Feng, H., Feldman, G., Franz, B., Frouin, R., Gould, R., Hooker, S., Kahru, M., Kratzer, S., Mitchell, B., Muller-Karger, F., Sosik, H., Voss, K., Werdell, J., Platt, T., 2019. An ocean-colour time series for use in climate studies: The experience of the ocean-colour climate change initiative (OC-CCI). Sensors 19 (19), 4285. http://dx.doi.org/10.3390/s19194285.

Sathyendranath, S., Brewin, R.J.W., Jackson, T., Mélin, F., Platt, T., 2017. Ocean-colour products for climate-change studies: What are their ideal characteristics? Remote Sens. Environ. 203, 125–138. http://dx.doi.org/10.1016/j.rse.2017.04.017.

Sathyendranath, S., Cota, G., Stuart, V., Maass, H., Platt, T., 2001. Remote sensing of phytoplankton pigments: A comparison of empirical and theoretical approaches. Int. J. Remote Sens. 22 (2–3), 249–273. http://dx.doi.org/10.1080/014311601449925.

Sathyendranath, S., Jackson, T., Brockmann, C., Brotas, V., Calton, B., Chuprin, A., Clements, O., Cipollini, P., Danne, O., Dingle, J., Donlon, C., Grant, M., Groom, S., Krasemann, H., Lavender, S., Mazeran, C., Mélin, F., Müller, D., Steinmetz, F., Valente, A., Zühlke, M., Feldman, G., Franz, B., Frouin, R., Werdell, J., Platt, T., 2021. ESA ocean colour climate change initiative (Ocean_Colour_cci): Version 5.0 Data. http://dx.doi.org/10.5285/1dbe7a109c0244aaad713e078fd3059a.

Sathyendranath, S., Platt, T., 2007. Spectral effects in bio-optical control on the ocean system. Oceanologia 49 (1), 5–39.

Sathyendranath, S., Platt, T., Irwin, B., Horne, E., Borstad, G., Stuart, V., Payzant, L., Maass, H., Kepkay, P., Li, W.K.W., Spry, J., Gower, J., 2004. A multispectral remote sensing study of coastal waters off Vancouver Island. Int. J. Remote Sens. 25 (5), 893–919. http://dx.doi.org/10.1080/0143116031000139836.

Sathyendranath, S., Platt, T., Kovač, Ž., Dingle, J., Jackson, T., Brewin, R.J.W., Franks, P., Marañón, E., Kulk, G., Bouman, H.A., 2020. Reconciling models of primary production and photoacclimation [Invited]. Appl. Opt. 59 (10), C100. http://dx.doi.org/10.1364/AO.386252.

Schaum, C.-E., Barton, S., Bestion, E., Buckling, A., Garcia-Carreras, B., Lopez, P., Lowe, C., Pawar, S., Smirnoff, N., Trimmer, M., Yvon-Durocher, G., 2017. Adaptation of phytoplankton to a decade of experimental warming linked to increased photosynthesis. Nat. Ecol. Evol. 1 (4), http://dx.doi.org/10.1038/s41559-017-0094.

Sharma, P., Marinov, I., Cabre, A., Kostadinov, T., Singh, A., 2019. Increasing biomass in the warm oceans: Unexpected new insights from SeaWiFS. Geophys. Res. Lett. 46 (7), 3900–3910. http://dx.doi.org/10.1029/2018GL079684.

Sieburth, J.M., Smetacek, V., Lenz, J., 1978. Pelagic ecosystem structure: Heterotrophic compartments of the plankton and their relationship to plankton size fractions 1. Limnol. Oceanogr. 23 (6), 1256–1263. http://dx.doi.org/10.4319/lo.1978.23.6.1256.

Siegel, D.A., Behrenfeld, M.J., Maritorena, S., McClain, C.R., Antoine, D., Bailey, S.W., Bontempi, P.S., Boss, E.S., Dierssen, H.M., Doney, S.C., Eplee, R.E., Evans, R.H., Feldman, G.C., Fields, E., Franz, B.A., Kuring, N.A., Mengelt, C., Nelson, N.B., Patt, F.S., Robinson, W.D., Sarmiento, J.L., Swan, C.M., Werdell, P.J., Westberry, T.K., Wilding, J.G., Yoder, J.A., 2013. Regional to global assessments of phytoplankton dynamics from the SeaWiFS mission. Remote Sens. Environ. 135, 77–91. http://dx.doi.org/10.1016/j.rse.2013.03.025.

Siegel, D.A., Franz, B.A., 2010. Century of phytoplankton change. Nature 466 (7306), 569–571. http://dx.doi.org/10.1038/466569a.

Smyth, T.J., Fishwick, J.R., AL-Moosawi, L., Cummings, D.G., Harris, C., Kitidis, V., Rees, A., Martinez-Vicente, V., Woodward, E.M.S., 2009. A broad spatio-temporal view of the Western English Channel observatory. J. Plankton Res. 32 (5), 585–601. http://dx.doi.org/10.1093/plankt/fbp128.

Sosik, H.M., Rynearson, T., Menden-Deuer, S., OOI CGSN Data Team, 2021. Size-fractionated chlorophyll from water column bottle samples collected during NES-LTER Transect cruises, ongoing since 2017. http://dx.doi.org/10.6073/pasta/798bda0e9ddfeba20f2266e64cf4dd40.

Southern California Bight MBON, Santa Barbara Coastal LTER, Catlett, D., Siegel, D., Guillocheau, N., 2021. Plumes and Blooms: Curated oceanographic and phytoplankton pigment observations ver 2. Environmental Data Initiative. http://dx.doi.org/10.6073/PASTA/12BD9B9805396ECEF006549144508124.

Stock, A., Subramaniam, A., 2022. Iterative spatial leave-one-out cross-validation and gap-filling based data augmentation for supervised learning applications in marine remote sensing. GISci. Remote Sens. 59 (1), 1281–1300. http://dx.doi.org/10.1080/15481603.2022.2107113.

Suggett, D.J., Moore, C.M., Hickman, A.E., Geider, R.J., 2009. Interpretation of fast repetition rate (FRR) fluorescence: signatures of phytoplankton community structure versus physiological state. Mar. Ecol. Prog. Ser. 376, 1–19. http://dx.doi.org/10.3354/meps07830.

Sun, X., Shen, F., Brewin, R.J.W., Li, M., Zhu, Q., 2022. Light absorption spectra of naturally mixed phytoplankton assemblages for retrieval of phytoplankton group composition in coastal oceans. Limnol. Oceanogr. http://dx.doi.org/10.1002/lno.12047.

Sun, X., Shen, F., Brewin, R.J.W., Liu, D., Tang, R., 2019. Twenty-year variations in satellite-derived chlorophyll-a and phytoplankton size in the bohai sea and yellow sea. J. Geophys. Res.: Oceans 124 (12), 8887–8912. http://dx.doi.org/10.1029/2019JC015552.

Sun, X., Shen, F., Liu, D., Bellerby, R.G.J., Liu, Y., Tang, R., 2018. In situ and satellite observations of phytoplankton size classes in the entire continental shelf sea, China. J. Geophys. Res.: Oceans 123 (5), 3523–3544. http://dx.doi.org/10.1029/2017JC013651.

Szeto, M., Werdell, P.J., Moore, T.S., Campbell, J.W., 2011. Are the world's oceans optically different? J. Geophys. Res.: Oceans 116 (C7), http://dx.doi.org/10.1029/2011JC007230.

Taylor, B.B., Bracher, A., 2017. Pigment concentrations measured in surface water during SONNE cruise SO202/2 (TRANSBROM). http://dx.doi.org/10.1594/PANGAEA.880235.

Taylor, B.B., Torrecilla, E., Bernhardt, A., Taylor, M.H., Peeken, I., Röttgers, R., Piera, J., Bracher, A., 2011. Pigments of phytoplankton during POLARSTERN cruise ANT-XXV/1. http://dx.doi.org/10.1594/PANGAEA.819070.

Tilstone, G.H., Land, P.E., Pardo, S., Kerimoglu, O., Van der Zande, D., 2023. Threshold indicators of primary production in the north-east Atlantic for assessing environmental disturbances using 21 years of satellite ocean colour. Sci. Total Environ. 854, 158757. http://dx.doi.org/10.1016/j.scitotenv.2022.158757.

Torrecilla, E., Stramski, D., Reynolds, R.A., Millán-Núñez, E., Piera, J., 2011. Cluster analysis of hyperspectral optical data for discriminating phytoplankton pigment assemblages in the open ocean. Remote Sens. Environ. 115 (10), 2578–2593. http://dx.doi.org/10.1016/j.rse.2011.05.014.

Turner, K.J., Mouw, C.B., Hyde, K.J.W., Morse, R., Ciochetto, A.B., 2021. Optimization and assessment of phytoplankton size class algorithms for ocean color data on the Northeast U.S. continental shelf. Remote Sens. Environ. 267, 112729. http://dx.doi.org/10.1016/j.rse.2021.112729.

Uitz, J., Claustre, H., Morel, A., Hooker, S.B., 2006. Vertical distribution of phytoplankton communities in open ocean: An assessment based on surface chlorophyll. J. Geophys. Res. 111 (C8), http://dx.doi.org/10.1029/2005JC003207.

Vaillancourt, R.D., Marra, J.F., 2011. Chlorophyll derived from HPLC from R/V Atlantic Explorer and R/V Cape Hatteras multiple cruises in the Sargasso Sea, Bermuda Atlantic Time Series (BATS) area, and Hydrostation S from 2007 to 2008 (ON DEQUE project). Biological and Chemical Oceanography Data Management Office (BCO-DMO), Version Date 2011-09-09.

Vidussi, F., Claustre, H., Manca, B.B., Luchetta, A., Marty, J.-C., 2001. Phytoplankton pigment distribution in relation to upper thermocline circulation in the eastern Mediterranean Sea during winter. J. Geophys. Res.: Oceans 106 (C9), 19939–19956. http://dx.doi.org/10.1029/1999JC000308.

Ward, B.A., 2015. Temperature-correlated changes in phytoplankton community structure are restricted to polar waters. In: Dam, H.G. (Ed.), PLOS ONE 10 (8), e0135581. http://dx.doi.org/10.1371/journal.pone.0135581.

Ward, B.A., Dutkiewicz, S., Jahn, O., Follows, M.J., 2012. A size-structured food-web model for the global ocean. Limnol. Oceanogr. 57 (6), 1877–1891. http://dx.doi.org/10.4319/lo.2012.57.6.1877.

Werdell, P.J., Bailey, S.W., Fargion, G.S., Pietras, C., Knobelspiesse, K.D., Feldman, G.C., McClain, C.R., 2003. Unique data repository facilitates ocean color satellite validation. EOS Trans. AGU 84 (38), 377.

Wernand, M.R., van der Woerd, H.J., Gieskes, W.W.C., 2013. Trends in ocean colour and chlorophyll concentration from 1889 to 2000, worldwide. In: Thompson, F. (Ed.), PLOS ONE 8 (6), e63766. http://dx.doi.org/10.1371/journal.pone.0063766.

Wu, L., Cai, W., Zhang, L., Nakamura, H., Timmermann, A., Joyce, T., McPhaden, M.J., Alexander, M., Qiu, B., Visbeck, M., Chang, P., Giese, B., 2012. Enhanced warming over the global subtropical western boundary currents. Nature Clim. Change 2 (3), 161–166. http://dx.doi.org/10.1038/nclimate1353.

Xi, H., Losa, S.N., Mangin, A., Garnesson, P., Bretagnon, M., Demaria, J., Soppa, M.A., d'Andon, O.H.F., Bracher, A., 2021. Global chlorophyll a concentrations of phytoplankton functional types with detailed uncertainty assessment using multisensor ocean color and sea surface temperature satellite products. J. Geophys. Res.: Oceans 126 (5), http://dx.doi.org/10.1029/2020JC017127.